MECCA

Journal of Middle European Construction and Design of Cars

Number 01 2021, volume XVIII. 165 Kč / 11€

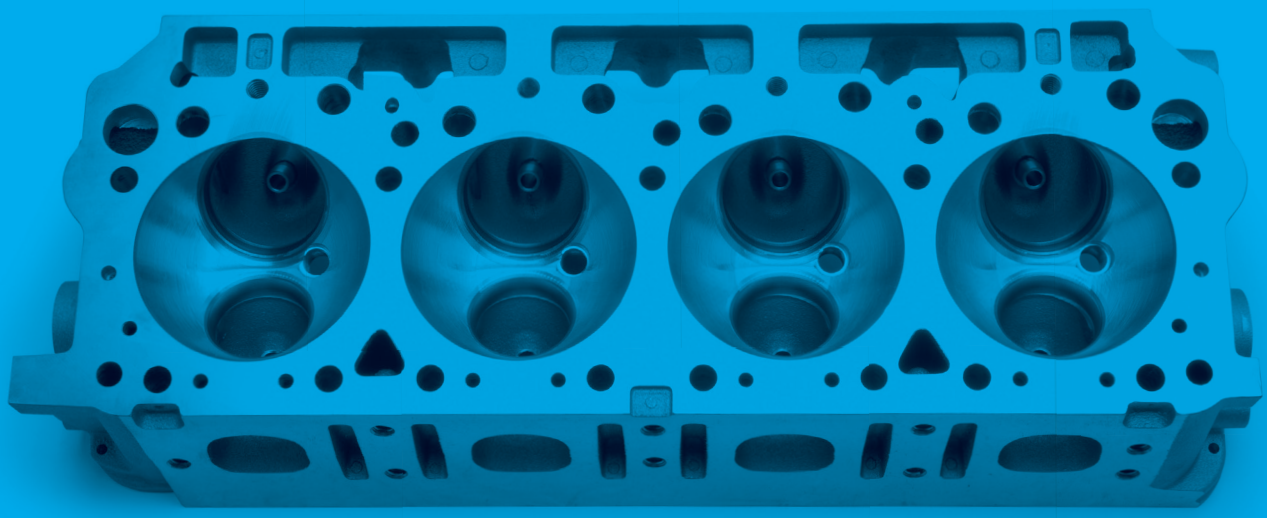

9 771214 082007

THIS ISSUE IS FOCUSED ON RESEARCH IN: DESIGN OF INTERNAL COMBUSTION ENGINES

AIM

Published in the heart of Europe on Czech Technical University in Prague the journal reports about research in the field of internal combustion engines and all other components and aspects of vehicle engineering and vehicle design. The articles from the whole world are welcome.

THE FOLLOWING TOPICS ARE RELEVANT FOR THE JOURNAL MECCA:

- Engines and fuels
- Powertrains (hybrid vehicles, transmissions,...)
- Chassis
- Vehicle body
- Experimental testing
- Mechatronics
- Vehicle dynamics
- Safety
- Transport Systems
- Electronics in vehicles

PERIODICITY

Three times a year

REVIEW PROCESS

All articles are peer and blind reviewed. At least two reviewers per article.

LANGUAGE

English, bilingual abstract and legends (English/Czech or English/Slovak). Articles coming from non-English speaking coutries are submitted to English correction.

ABSTRACTING AND INDEXING

The journal is part of database of open access publications (DOAJ): https://doaj.org/toc/1804-9338

MEMBERS OF EDITORIAL BOARD

EDITOR IN CHIEF
Prof. Ing. Jan Macek, DrSc.
Czech Technical University, Prague, CZ
Technická 4, Praha 6, 16607, Czech republic

SENIOR EDITOR
doc. Dr. Ing. Gabriela Achtenová Czech Technical University, Prague, CZ
JUNIOR EDITOR
Ing. JAROSLAV KANĚRA Czech Technical University, Prague, CZ

EDITORIAL BOARD
Prof. Dr. Ing. Milan APETAUR Technical University Ústí nad Labem, CZ
Dr. Ing. Eduardo Jose BARRIENTOS Czech Technical University in Prague, CZ
Prof. Dr. Ing. Stanislav BEROUN Technical University Liberec, CZ
Dr. Ing. Yann MARCO Ensieta, France
Prof. Dr. Vladimir MEDICA University of Rijeka, Croatia
Dr. Ing. Tamás MERÉTEI Institute for Transport Sciences Ltd., Hungary
Ing. Antonín MIKULEC Czech Technical University, Prague, CZ
Dr. Ing. Thomas MOREL Gamma Technologies, USA
Prof. Dr. Ir. Joop PAUWELUSSEN HAN University, Tle Netherlands
Prof. Dr. Ing. Václav PÍŠTĚK Brno University of Technology, CZ
Doc. Dr. Ing. Miloš POLÁŠEK Porsche Engineering Services, CTU Prague, CZ
Doc. Dr. Marián POLÓNI Slovak University of Technology, Slovakia
Dr. Ing. Vladimír ŠATOCHIN Motor Vehicle Research Institute Ltd., CZ
Dr. Ing. Václav TAJZICH Motor Vehicle Research Institute Ltd., CZ
Prof. Dr. Ing. Michal TAKÁTS Czech Technical University, Prague, CZ
Prof. Dr. Ing. Michael VALÁŠEK Czech Technical University, Prague, CZ
Dr. Ing. Jiří VÁVRA University of Michigan, Michigan, USA
Dr. Ing. Oldřich VÍTEK Czech Technical University, Prague, CZ
Ing. Jan WANGLER formerly Praga, a.s., CZ

This journal is published using financial support from the budget of the Centre of Vehicles for Sustainable Mobility, Faculty of Mechanical Engineering, Czech Technical University in Prague. A part of support comes from the project Josef Božek Competence Centre for Automotive Industry TE 0102 0020, funded by the Technological Agency of Czech Republic. These sources are gratefully acknowledged.

IMPRINT MECCA – VOLUME XVIII, NUMBER 01, YEAR 2021, https://ojs.cvut.cz/ojs/index.php/mecca, gabriela.achtenova@fs.cvut.cz
Publisher: CTU in Prague and Centre of Vehicles for Sustainable Mobility, Technická 4, 16607, Praha 6, Czech republic, **ISSN 1214-0821, ISSN 1804-9338 (Online), MK ČR E 13720 Proofreading:** Channel Crossings, Prague, Czech Republic **Advertising:** gabriela.achtenova@fs.cvut.cz or jan.macek@fs.cvut.cz
Production/Layout: studio pixle (studio@pixle.cz)

10.14311/mecdc.2021.01.01

CRITICAL SHIFTING WINDOW IN SWITCHABLE ROCKER FINGER FOLLOWER

PETR KOHOUT
Eaton European Innovation Center, Bořivojova 2380, 252 63 Roztoky, Email: petrkohout@eaton.com
JAN KINDERMANN
Eaton European Innovation Center, Bořivojova 2380, 252 63 Roztoky, Email: jankindermann@eaton.com

ABSTRACT
A valvetrain including switchable rocker finger follower is capable of discrete switching between two modes (two cam profiles). The exact moment when switching occurs is called crossover point and this paper reviews the factors that cause the shift of the crossover point from its nominal design position. The range where crossover point can shift is called critical shifting window and its size and factors influencing it will be adressed.
KEYWORDS: CAM, CAM PROFILE, CAM DESIGN, SWITCHABLE ROLLER FINGER FOLLOWER, TOLERANCES, STACK UP, SHIFTING WINDOW, CAE

SHRNUTÍ
Ventilový rozvod s přepínatelným vahadlem s rolnami je schopen přepínat mezi dvěma režimy (přepínání mezi dvěma vačkovými profily). Okamžik, kdy dojde k přepnutí mezi jednotlivými vačkami, se nazývá bod přechodu. V tomto příspěvku budou uvedeny jednotlivé faktory, které způsobují posun bodu přechodu z jeho jmenovité návrhové pozice. Celý rozsah kam se může bod přechodu posunout je označován jako okno bodu přechodu a v příspěvku bude probráno jak jednotlivé faktory ovlivňují jeho velikost.
KLÍČOVÁ SLOVA: VAČKA, PROFIL VAČKY, NÁVRH VAČKY, PŘEPÍNATELNÉ VAHADLO S ROLNAMI, TOLERANCE, TOLERANČNÍ ANALÝZA, OKNO PŘECHODU, CAE

1. INTRODUCTION

Valvetrain mechanism between camshaft and a valve itself allows to transform camshaft rotational movement to the intake and exhaust valve translational movement. The conventional and simplest valvetrain operation allows the fresh air or air-fuel mixture to enter the cylinder during the intake stroke when intake valves are open, participate on combustion and let the combustion products leave the cylinder during exhaust stroke when exhaust valves are open. But as demands on engines increase and fulfilling prescribed emission limits is more and more challenging new technologies and innovation are being used. The valvetrain is no exception and variable valve timing (VVT) and variable valve lift (VVL) are used in vehicles nowadays. Cam phaser is the most common way for VVT implementation. It allows to shift the entire valve lift within the specified range of an engine cycle and it appears in two versions – discrete and continuous timing switching. Switching between different cams is used for the VVL realization. The axial camshaft shifting or switching the cam that controls the valve using advanced finger followers or rocker arms is used by OEMs. Combination of VVT and VVL is commonly called as variable valve actuation (VVA). Different VVA systems used by OEMs are usually called by their marketing name such as VTEC, VANOS, MultiAir, MIVEC etc. Camless valvetrains are the most variable solution but they are used mainly in experimental and research engines so far [1]. More on the topic of VVA can be found in the following publications – [2], [3], [4]. The switchable roller finger follower (SRFF) is one of the ways how to implement discrete variable valve lift. [5] That means it allows to switch between two different valve lifts. The crossover point is the moment when switch is realized, thus the moment when the valve changes cam lobe which prescribes its lift. The principle of SRFF will be explained followed by the thorough description of the critical shifting window, how it is created and influence of the specific factors on the window size.

2. SWITCHABLE ROLLER FINGER FOLLOWER VALVETRAIN

The conventional valvetrain system with a standard roller finger follower shown in Figure 1 is often referred to as Type II valvetrain. It consists of a camshaft that acts on a roller finger follower through its roller. The roller finger follower is in contact with pivot on one side and valve stem on the other side. Improvement of such a system by replacing the roller finger follower by its switchable version (Figure 2) enables to switch between two different lifts on one valve. It allows to switch for example between normal mode and Miller cycle on the intake side.

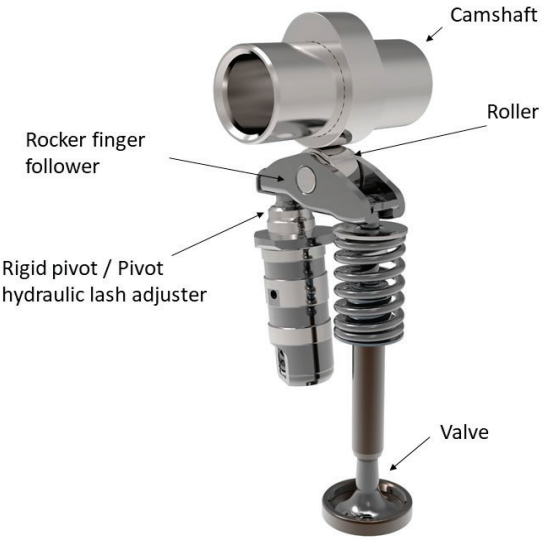

FIGURE 1: Type II valvetrain
OBRÁZEK 1: Ventilový rozvod typ II

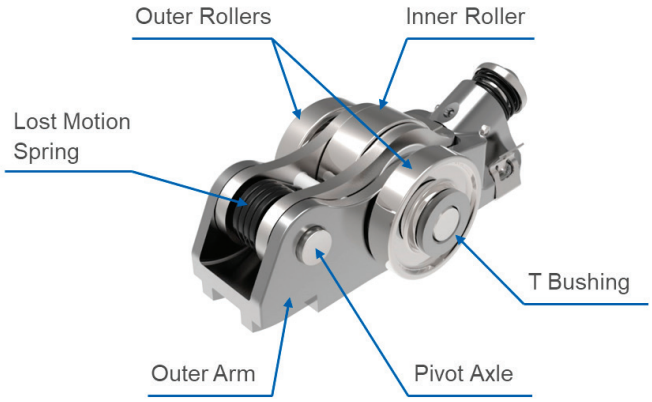

FIGURE 2: Switchable rocker finger follower (SFRR)
OBRÁZEK 2: Přepínatelné vahadlo

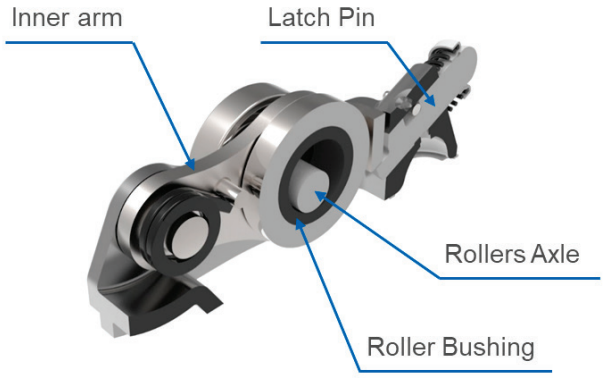

FIGURE 3: SRFF section
OBRÁZEK 3: Řez vahadlem

The same thing could be applied to the exhaust side where normal exhaust valve lift can be supplemented by small extra lift during the intake stroke, which allows to get some of the exhaust gases entering back to the cylinder and this is often referred to as internal exhaust gas recirculation (iEGR). SRFF can be used for cylinder deactivation or other advanced valve actuation strategies.

Inside the SRFF there is a latch pin (Figure 3) and depending on its position the finger follower responds to the inner roller. When the pin is not latched the inner roller of SRFF makes so called lost motion. On the other hand, when the pin is latched the entire SRFF and thus also the valve reacts on the movement of the inner roller. To be able to perform two different lifts with SRFF valvetrain system a camshaft must have 3 cam lobes per SRFF (Figure 4). Two outer cam lobes are identical and act on outer rollers of the SRFF,

FIGURE 4: SRFF cam lobes
OBRÁZEK 4: Vačky pro přepínatelné vahadlo

the inner cam lobe acts on inner roller which is connected to the inner arm and can either perform a lost motion or transmit the cam lift into the valve lift. Function of SRFF valvetrain when the pin is not latched is as follows. On the base circle the outer cam lobes are in contact with outer roller (no lash is present because a hydraulic lash adjuster is often used). The lash between the inner cam lobe and the inner roller is present and is called mechanical lash at cam (MLC). As the camshaft rotates the valve lift is influenced only by outer cam lobes. During the camshaft rotation there is a moment when inner cam lobe gets in contact with inner roller and as MLC gets closed the impact on inner roller appears. The lift is not transferred from the inner cam lobe to the valve as pin is not latched and inner arm makes lost

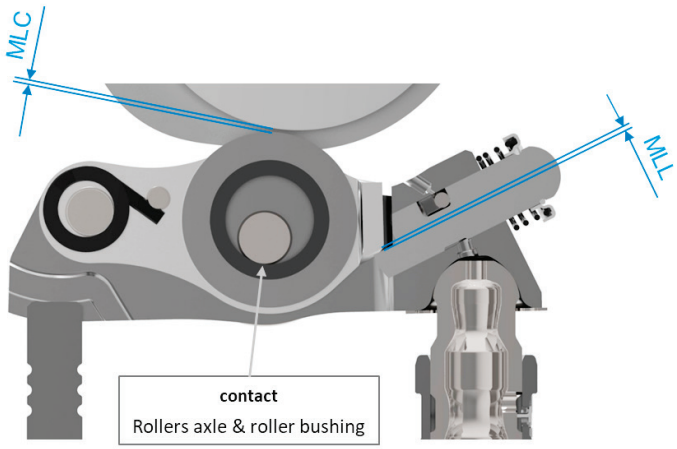

FIGURE 5: Mechanical lashes in the SRFF
OBRÁZEK 5: Vůle v přepínatelném vahadle

motion. When pin is latched the situation in the beginning is similar. Outer rollers are in contact with cam lobes, MLC is present and there is also lash between latch pin shelf and inner arm mating surface which is called mechanical lash at latching pin (MLL). During the camshaft rotation the MLC is closed first, then the inner arm starts to move and MLL is closed. At this moment the valve lift is no more controlled by the outer lobe profiles and starts to be controlled by the inner lobe profile instead. This moment is considered as the crossover point. Very similar conditions and phenomena as during crossover point happen when MLC is closed so further in the article it will be adressed as a crossover point 1 (CP1) and the actual crossover point when MLL is closed as crossover point 2 (CP2). As the lift of the inner cam lobe decreases back to the base circle, the MLL is opened first and outer cam lobes get in contact with outer rollers and valve is again controlled by the them. Further as the inner cam lobe lift goes back to base circle the MLC is opened.

3. APPROACH

GT-Suite is a CAE toolset widely used in industry especially in the automotive as it has many useful features for simulation of the specific parts of the vehicles and engines. It is capable of 1-D flow simulation, kinematics, MBD etc.. Two parts of this complex software package were used in order to examine influence of various factors on width of critical shifting window. The GT-ISE where libraries for valvetrain and multibody dynamics were used and VTDESIGN where cam profiles were designed, and kinematics of the system was examined. In general, when designing cam profile, it is important to control cam velocity and acceleration. Too high velocity during opening and closing ramps results in excessive impacts in the system which result in increased wear or higher failure probability. Acceleration is controlled in order to avoid contact separation in the valvetrain. A separation could happen when inertia forces are higher than force generated by a valve spring. Acceleration has a direct influence on manufacturability as with the high acceleration the concave radius of curvature of the cam decreases. If cam concave radius is smaller than the grinding tool, it will be impossible to grind some areas on the profile. Specific limit values are usually set by internal company guidelines and are often treated as business secret. More about process of developing the cam profile can be found in [6]. The MBD model of the single valve mechanism including SRFF was built in GT-ISE in such a way that position of various components in the valvetrain can be quickly and easily changed which allows to implement manufacturing tolerances and wear of the specific parts in the system. VTDESIGN was used to design cam lobe profiles which are then input in the MBD model. Initially the simulation was performed with all the nominal dimensions and baseline cam profiles thus perfectly fulfilling the moment when CP1 and CP2 were intended to happen based on the specific requirements on the function of the valvetrain and engine. Furthermore, the position of the components was changed in order to simulate influence and sensitivity of moment CP1 and CP2 on manufacturing tolerances and other aspects that will be discussed later in appropriate chapters followed by the interpretation of the results and conclusion. The main motivation for keeping critical shifting window small is because only in this area the crossover point can happen thus only here the velocity difference needs to be controlled. If the CSW is too wide the velocity difference needs to be kept sufficiently small for a long time period and that results in restrictions for cam design of inner and outer cam lobe profile.

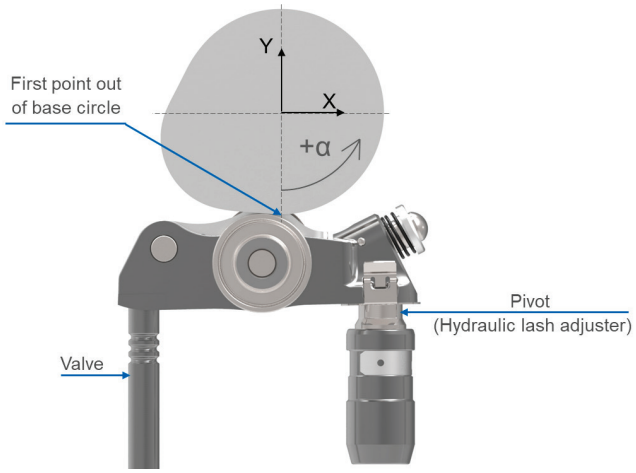

FIGURE 6: Simulation initial state
OBRÁZEK 6: Počáteční stav simulací

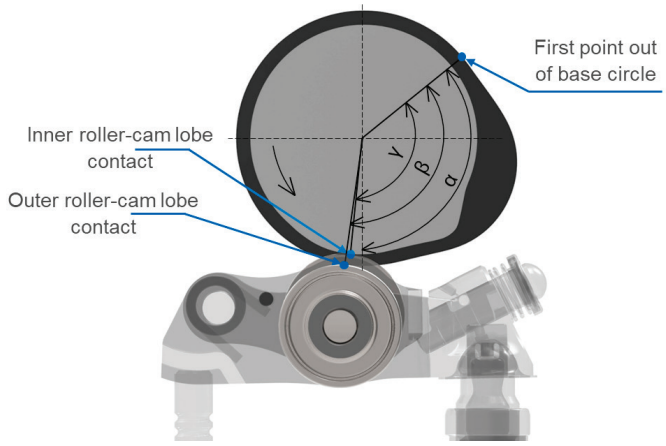

FIGURE 7: Crossover point angles definition
OBRÁZEK 7: Definice úhlů pro bod přechodu

4. BASELINE

The MBD simulation using all the nominal dimensions was performed in order to set the nominal position of the CP1 and CP2. The critical shifting window will be created around those values as different factors will be changed in the following chapters. It is also important to set up the initial position of every simulation and derived angular positions of contacts during the CP. Every simulation performed has the same layout as specified in Figure 6. From the point of view, the valve is on the left and pivot on the right, the camshaft rotates counterclockwise and all the cam lobe first points (first point that is higher than cam base circle) lies on the global negative Y axis. As the simulation time goes forward the camshaft rotates and angles α, β, γ can be observed as in Figure 7. α is the angle between negative Y axis and the cam lobe first point and gives us the information about the timing. It tells when the CP happens. β is the angle between first cam lobe point and the contact point between outer cam and roller. It gives us the information about where on outer cam profile does the CP happen. γ is very similar to β but it goes from the first point of the cam lobe to the contact of inner cam and roller.

All three angles will be used in description of the critical shifting windows. Big deviation in α signs that the function of the inner profile lift can cause not desired influence on the engine cycle as the prescribed CP can happen too early or too late. Angles β and γ gives us the information where is the contact point on the cam when the CP happens. It is important as it gives us the information about the impact that appears in the system during CP. In order to realize CP, the velocity on the inner cam lobe has to be higher than on outer cam lobe so the lashes will get closed. But the velocity difference has to be limited so the strong impacts will not damage and wear the components and cause the system failure.

TABLE 1: Nominal crossover points
TABULKA 1: Nominální přechodové body

Baseline CP1			Baseline CP2		
α [deg]	β [deg]	γ [deg]	α [deg]	β [deg]	γ [deg]
87,8	91,3	91,1	101,9	102,7	101,9

TABLE 2: Baseline relative velocity difference during crossover point
TABULKA 2: Výchozí relativní rozdíl rychlostí na vačkách v přechodových bodech

Baseline CP1 vel. difference [mm/deg]	Baseline CP2 vel. difference [mm/deg]
0,0075	0,0075

Relative velocity difference is calculated as described in equation (1) and (2).

$$v_{diff@CP1} = v_{inner}(\gamma_{CP1}) - v_{outer}(\beta_{CP1}) \quad (1)$$

$$v_{diff@CP2} = v_{inner}(\gamma_{CP2}) - v_{outer}(\beta_{CP2}) \quad (2)$$

Baseline design angles α, β, γ are in the Table 1 and relative velocity difference inTable 2.

CP1 happens when camshaft rotates 87,8° from the initial position and rollers are in contact at 91,3° of outer cam lobe and 91,1° of inner camlobe. CP2 design moment is at 101,9° rotation after initial state. Outer cam lobe is in contact with roller at 102,7° of its profile and inner cam lobe at 101,9° of its profile. Critical shifting window will be created around those nominal values. Same cam lobe profiles will be used if not mentioned otherwise.

5. SRFF TOLERANCE FACTORS

In an ideal case every product going from the same production line would be identical. But in practice even if material goes through same prescribed set of operations there is always some deviation in dimensions or material properties thus the final products have some level of variation. But that does not necessarily mean that the function is affected. Setting the tolerances for manufacturing processes limits the deviation in final products in a way that desired function is assured. But setting the tolerance limits has its other side as well. The tighter are the deviation limits the more accurate thus more costly steps and processes must be utilized. It is always extremely important to find a compromise between the price and tolerance levels. All the component variations are taken in account in so called stack-up analysis to see if the desired function is assured. The stack-up analysis is not the object of interest in this article thus it will not be described in detail what is the cause of position change. Only the stack--up analysis results of parts that affects the critical shifting window will be used. Some of the cases that are discussed are artificially created but it helps to distinguish what is the real factor that moves a crossover point. It can be observed for example in first case where x position of outer rollers is changed. In real scenario the resulting change in position of outer roller would be caused by changed position of the outer roller axis and as this axis is in contact with bushing of the inner roller it would naturally change the initial position of inner roller and size of MLC. For sake of clarity and simplicity let's consider cases where only one specific position is changed and rest stays in its nominal position.

TABLE 3: Results for different outer rollers position
TABULKA 3: Výsledky pro různé pozice vnějších rolen

Outer roller position tolerance		CP1			CP2		
X tol [mm]	Y tol [mm]	α [deg]	β [deg]	γ [deg]	α [deg]	β [deg]	γ [deg]
0	0	87,8	91,3	91,1	101,9	102,7	101,9
-0,03	0	86,4	90,4	90,0	100,4	101,5	100,6
-0,02121	0,02121	88,8	92,1	91,8	102,9	103,7	102,8
0	0,03	90,8	93,6	93,3	105,1	106,0	105,0
0,02121	0,02121	91,0	93,8	93,5	105,1	105,9	105,0
0,03	0	89,3	92,4	91,2	103,4	104,1	103,2
0,02121	-0,02121	86,7	90,3	90,2	100,9	101,8	101,1
0	-0,03	84,7	88,7	88,6	99,2	100,4	99,7
-0,02121	-0,02121	84,5	88,6	88,5	99,0	100,2	99,5

5.1 OUTER ROLLERS POSITION

Influence of roller position tolerance was examined in 9 cases prescribed as in Figure 8– 1 nominal position and then 8 positions of the outer roller axis on the circle with radius of 0.03 mm.
Results are in Table 3 and it can be seen that values for α (the angle describing the timing) go from 84,5° to 91° for CP1 and from 99° to 105,1° for CP2. If it is considered that 1° of cam angle rotation corresponds to 2° of crank angle (CA) rotation the shift of the CP1 in engine cycle can be shown. CP1 can happen 6,6° CA before or 6,4° CA after the designed moment and anywhere in between. CP2 can happen 5,8° CA before or 6,4° CA after the designed moment and anywhere in between. In the next chapters the result description will not be as detailed as here, but only table with results and critical shifting window expressed by the range of α will be mentioned.

5.2 INNER ROLLER POSITION

The same strategy as in the previous chapter was used and 9 cases were simulated including nominal position and 8 axis offset positions on a circle around the nominal position (Figure 9).

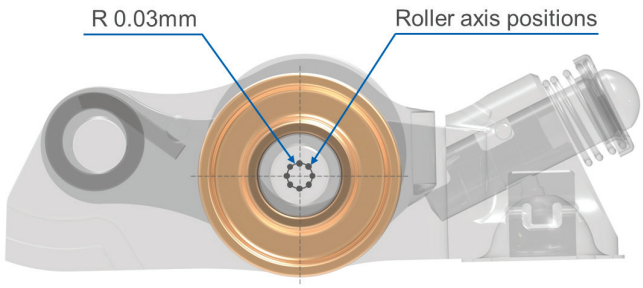

FIGURE 8: Examined outer rolers axis positions
OBRÁZEK 8: Zkoumané pozice osy vnějších rolen

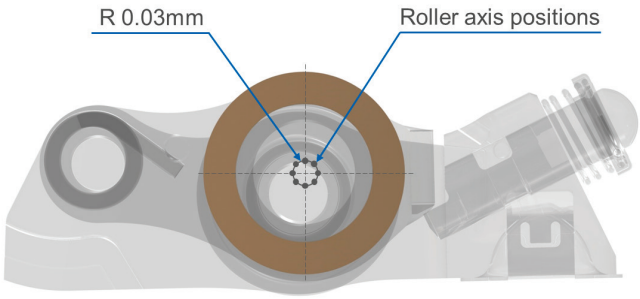

FIGURE 9: Examined inner rolers axis positions
OBRÁZEK 9: Zkoumané pozice osy vnitřních rolen

TABLE 4: Results for different inner rollers position
TABULKA 4: Výsledky pro různé pozice vnitřních rolen

Inner roller position tolerance		CP1			CP2		
X tol [mm]	Y tol [mm]	α [deg]	β [deg]	γ [deg]	α [deg]	β [deg]	γ [deg]
0	0	87,8	91,3	91,1	101,9	102,7	101,9
-0,03	0	89,3	92,5	92,2	103,4	104,1	103,3
-0,02121	0,02121	86,6	90,3	90,2	101,0	101,9	101,1
0	0,03	84,7	88,8	88,7	99,2	100,4	99,7
0,02121	0,02121	84,5	88,6	88,5	99,0	100,2	99,5
0,03	0	86,4	90,1	89,9	100,5	101,5	100,6
0,02121	-0,02121	88,8	92,1	91,8	102,9	103,7	102,7
0	-0,03	90,7	93,6	93,3	105,1	105,9	104,9
-0,02121	-0,02121	91,0	93,8	93,5	105,1	105,9	105,0

Critical shifting window influenced only by the inner roller position goes from 84,5° to 91° in terms of α for CP1 and from 99° to 105,1° for CP2.

5.3 LATCH-PIN SHELF TOLERANCE

When referring to the latch-pin shelf tolerance, the position of surface compared to nominal position as shown in Figure 10 is meant. As this dimension is not anyhow involved during the CP1 its influence only on CP2 will be examined.

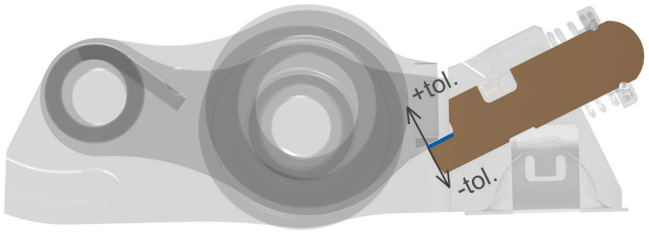

FIGURE 10: Latch-pin shelf tolerance
OBRÁZEK 10: Tolerance obrobení plochy přepínacího čepu

TABLE 5: Reults for latch-pin shelf tolerance
TABULKA 5: Výsledky pro tolerance plochy přepínacího čepu

Pin tolerance	CP2		
[mm]	α [deg]	β [deg]	γ [deg]
0	101,9	102,7	101,9
-0,03	100,0	101,0	100,3
-0,02	100,5	101,5	100,7
-0,01	101,2	102,1	101,3
0,01	102,6	103,4	102,5
0,02	103,4	104,1	103,2
0,03	104,1	104,9	103,9

The critical shifting window for CP2 in term of α can go from 100° to 104,1° due to the latch-pin shelf tolerance.

6. CAM LOBE TOLERANCES

The same as for SRFF is valid for the cam lobe profiles. The tolerances that are taken in account here are cam profile tolerance, wear and cam profile angular tolerance. Profile tolerance is easy to understand as it means that the designed cam profile can be either higher or lower by the specified value. Wear is captured by adding higher value to the negative side of the profile tolerance so the actual cam profile can be lower than the nominal partially because of manufacturing and partially due to wear over the time. Cam angular tolerance means that the cam lobe profile can be shifted relatively to the other cam lobe. In the baseline case, both cam lobes have their first profile point in the direction of negative Y direction but in reality, the profiles can be shifted to each other due to angular position tolerance

6.1 OUTER CAM LOBE PROFILE TOLERANCE

Four cases were tested including again the nominal dimension, then two cases for ±0,03 caused by the manufacturing and then case -0,06 where the half of the value is caused by the manufacturing and half by the wear of the cam lobe. Thus the tested cases and critical shifting window are not symmetrical. Each case results are Table 6.
Critical shifting window influenced only by outer cam profile tolerance and wear goes from 80,3° to 91° in terms of α for CP1 and from 96,4° to 105,0° for CP2.

TABLE 6: Results for outer cam profile tolerance and wear
TABULKA 6: Výsledky pro profilovou toleranci a opotřebení vnějších vaček

Outer cam profile tolerance	CP1			CP2		
[mm]	α [deg]	β [deg]	γ [deg]	α [deg]	β [deg]	γ [deg]
0	87,8	91,3	91,1	101,9	102,7	101,9
-0,06	80,3	85,2	85,2	96,4	98,0	97,5
-0,03	84,5	88,6	88,5	99,0	100,2	99,5
0,03	91,0	93,8	93,5	105,0	105,9	105,0

6.2 INNER CAM LOBE PROFILE TOLERANCE

The same cases as in previous chapter were tested for the inner cam lobe tolerances. Results are in the Table 7.
Critical shifting window influenced only by inner cam profile tolerance and wear goes from 84,5° to 91° in terms of α for CP1 and from 99,3° to 105,1° for CP2. The trend is here opposite to the

TABLE 7: Results for inner cam profile tolerance and wear
TABULKA 7: Výsledky pro profilovou toleranci a opotřebení vnitřní vačky

Inner cam profile tolerance [mm]	CP1			CP2		
	α [deg]	β [deg]	γ [deg]	α [deg]	β [deg]	γ [deg]
0	87,8	91,3	91,1	101,9	102,7	101,9
-0,06	93,9	96,1	95,6	108,5	110,9	110,0
-0,03	91,0	93,8	93,5	105,1	105,9	105,0
0,03	84,5	88,6	88,5	99,3	100,4	99,7

tolerances of outer cam lobe. The higher is the inner cam profile the earlier happen both crossover points while at the outer cam lobe the higher is the profile the later the crossover points occur.

6.3 OUTER CAM LOBE ANGULAR TOLERANCE

Changing the relative angular position of the cams means shifting the profile timing thus changing all the cam lobe characteristics including lift, velocity and other higher derivatives. It is important to check if the relative velocity difference during CP do not exceed the prescribed guideline limits so the impacts in the system are controlled. Results for outer cam lobe angle are in Table 8.
Critical shifting window influenced only by outer cam angular tolerance goes from 83,2° to 93,9° in terms of α for CP1 and from 95,9° to 108,5° for CP2.

TABLE 8: Results for angular tolerance of outer cam lobes
TABULKA 8: Výsledky pro úhlovou toleranci vnějších vaček

Outer cam angular tolerance [deg]	CP1			CP2		
	α [deg]	β [deg]	γ [deg]	α [deg]	β [deg]	γ [deg]
0	87,8	91,3	91,1	101,9	102,7	101,9
-0,5	83,2	88,0	87,5	95,9	98,1	97,1
0,5	93,9	95,7	95,7	108,5	109,5	109,3

TABLE 9: Results for angular tolerance of inner cam lobe
TABULKA 9: Výsledky pro úhlovou toleranci vnitřní vačky

Inner cam angular tolerance [deg]	CP1			CP2		
	α [deg]	β [deg]	γ [deg]	α [deg]	β [deg]	γ [deg]
0	87,8	91,3	91,1	101,9	102,7	101,9
-0,5	93,4	95,7	95,7	108,0	109,5	109,3
0,5	83,7	88,0	87,5	96,4	98,1	97,1

6.4 INNER CAM LOBE ANGLE POSITION TOLERANCE

Same cases as prescribed in previous chapter were tested for inner cam lobe angular tolerance. See the results in the Table 9. Critical shifting window influenced only by inner cam angular tolerance goes from 83,7° to 93,4° in terms of α for CP1 and from 96,4° to 108,0° for CP2. It can be observed that the trends are similar as in cam lobe profile tolerance – shifting outer cam lobe angular position clockwise (+0,5°) cause CPs occur later on the other hand shifting the inner cam lobe same direction causes that CPs occur earlier.

7. WORST CASE SCENARIO

After the examination of each factor influence to the position of CPs the overall impact of all should be added together and see how it can influence the moment of CP1 and CP2. In reality such a case is highly improbable and statistical approach should be applied so the tolerances are not set too strict only for highly improbable combinations. See the results in Table 10.

TABLE 10: Worst case scenario results
TABULKA 10: Výsledky pro kombinaci nejhorších možných tolerancí

Worst case superposition	CP1			CP2		
	α [deg]	β [deg]	γ [deg]	α [deg]	β [deg]	γ [deg]
Beginning of CSW	63,8	72,0	71,6	78,2	83,9	83,1
End of CSW	110,5	112,4	113,3	120,3	126,0	127,5

It can be observed that due to manufacturing tolerances set as prescribed in the previous chapters the CP1 can happen anytime from 63,8° to 110,5° and CP2 from 78,2° to 120° in terms of α. Critical shifting window is 46.7° wide for CP1 and 42,1°wide for CP2. Such a width of CSW and level of uncertainty when does the CP happen might not be sufficient for some applications so in the next chapter there will be ways how to influence the the width of CSW.

8. CRITICAL SHIFTING WINDOW ADJUSTMENTS

There are two ways how to adjust the width of CSW. First way is very obvious, and it consists of making tolerances tighter. For our case the tolerances were halved. It can be considered that for roller tolerances the more accurate machine was used to drill the holes in SRFF, and more precise turning was used for rollers. That would result in roller's axis lying in circle of radius 0,015mm around its nominal position. Same applies for cam tolerances,

TABLE 11: Results for worst case scenario with half tolerances
TABULKA 11: Výsledky pro kombinaci nejhorších možných polovičních toleranci

Worst case with half tolerances	CP1			CP2		
	α [deg]	β [deg]	γ [deg]	α [deg]	β [deg]	γ [deg]
Beginning of CSW	75,0	81,1	80,8	89,3	92,6	91,9
End of CSW	101,2	101,9	101,5	114,7	119,2	119,8

furthermore the better material in terms of wear would be used so the peak wear decreases to 0,015mm thus cam profile tolerance would go from -0,03 mm to +0,015 mm around nominal value and cam angle tolerance ±0,25°. Influence on CSW is in Table 11.

The improvement is significant and CSW for CP1 goes from 75° to 101,2° and for CP2 from 89,3° to 114,7° in terms of α. Then width of the CSW is 26,2° for CP1 and 25,4° for CP2.

Another way how to make CSW tighter is the adjustment of cam design and its velocity specifically. Tolerance deviation is basically increasing or decreasing the initial size of the lashes (MLC, MLL) compared to nominal, which has to be closed. The relative velocity difference tells us how quickly get those lashes closed around CP. Adjusting cam design in a way that position of CP stays the same but relative velocity difference is higher will result in closing the lashes with their deviations faster and

TABLE 11: Results for worst case scenario with half tolerances
TABULKA 11: Výsledky pro kombinaci nejhorších možných polovičních toleranci

Worst case with half tolerances	CP1			CP2		
	α [deg]	β [deg]	γ [deg]	α [deg]	β [deg]	γ [deg]
Beginning of CSW	75,0	81,1	80,8	89,3	92,6	91,9
End of CSW	101,2	101,9	101,5	114,7	119,2	119,8

TABLE 12: Higher relative velocity difference for new inner cam
TABULKA 12: Vyšší relativní rozdíl rychlostí pro novou vnitřní vačku

Higher CP1 vel. difference [mm/deg]	Higher CP2 vel. difference [mm/deg]
0,0103	0,0132

TABLE 13: Results for new inner cam with higher relative velocity difference
TABULKA 13: Výsledky pro novou vnitřní vačku s vyšší relativní rychlostí

Higher cam velocity difference	CP1			CP2		
	α [deg]	β [deg]	γ [deg]	α [deg]	β [deg]	γ [deg]
Beginning of CSW	68,5	75,9	75,7	84,7	89,2	88,6
End of CSW	102,3	102,6	102,6	116,2	120,9	121,8

so decreasing the influence of tolerances on CSW size. The new inner cam profile was designed wither higher relative velocity difference (Table 12) and its influence on CSW size is in Table 13. The results show the size of CSW can be decreased by proper cam design as well. In this case increasing relative velocity difference for CP1 from 0,0075 mm/deg to 0,0103 mm/deg decreased the size of CSW by 12,9° in terms of α. With velocity difference increase from 0,0075 mm/deg to 0,0132 mm/deg for CP2 the CSW was decreased by 10,6° in terms of α. Increasing relative velocity is not for free as well, since the higher the difference is the higher is the impact that appears in the system during CP. The advantage of making CSW tighter has to be compared with disadvantage of possible higher wear or necessity of using better material.

Last case in this article will be the combination of two adjustments made above. The results for case where tolerances have the half size compared to the worst case and the relative velocity difference is as in Table 12.

TABLE 14: Results for half tolerances and higher relative velocity difference
TABULKA 14: Výsledky pro poloviční tolerance a vyšší relativní rychlost mezi vačkami

Worst case with tighter tolerance and higher velocity difference	CP1			CP2		
	α [deg]	β [deg]	γ [deg]	α [deg]	β [deg]	γ [deg]
Beginning of CSW	79,9	85,1	84,8	92,5	95,1	94,4
End of CSW	96,1	97,6	97,2	110,2	112,3	111,5

Critical shifting window is 16,2° wide for CP1 and 17,7° wide for CP2 in terms of α.

9. CONCLUSION

Concept and principle of critical shifting window was explained and influence of various factors on its size was examined. Detailed study of each factor was performed and based on results the following can be stated. The presence of critical shifting window is inevitable, and its size is prescribed by the manufacturing tolerances and design of a cam lobe profile during CP. Adjustments to the size of CSW can be done either by making manufacturing process more accurate or by increasing the relative velocity difference at cam lobes during the CP. The disadvantage of more accurate manufacturing process is the higher cost. The information about the actual tolerance classes, tolerance-based assembly and the trade-off between cost and CSW width is usually considered as a business secret and it is extremely difficult to reach to such information. It is important to compare the brought advantage for the increased cost. For example, if improving production process of the camshaft would

bring the same benefit as improving the accuracy of rollers position but the cost is rapidly higher for the camshaft then focusing on SRFF manufacturing process is the way to go to. The increased relative velocity difference has also its disadvantage because the higher is the velocity difference the higher are the impacts in the system and higher wear can occur. The influence of the tolerances to a valve lift change and to the engine breathing was not the area of interest for this paper but as the values of tolerances are in hundredths of millimetres it is expected to have minor or almost no influence to the engine performance.

REFERENCES

[1] Kisabo A.B., Ibrahim M. J., Oluwafemi O. A., Comparative Analysis Between Cam and Cam-less Valve Actuating for Automotive System. International Journal of Systems Engineering, Vol. 1, No. 2, 2017, pp. 48–57. doi: 10.11648/j.ijse.20170102.12

[2] Lou Z., Zhu G., Review of Advancement in Variable Valve Actuation of Internal Combustion Engines. Applied Science. 2020, 10(4), 1216, 2020, doi:10.3390/app10041216.

[3] J. R., Variable Valvetrain System Technology, SAE International, 2006, ISBN 978-0-7680-1685-7

[4] Norton L.R., Cam Design and Manufacturing Handbook – 2nd edition Reference Book, Industrial Press Inc., 2009, ISBN-13: 978-0831133672

[5] Radulescu, A., McCarthy JR, J., and Brownell, S., Development of a Switching Roller Finger Follower for Cylinder Deactivation in Gasoline Engine Applications, SAE Technical Paper 2013-01-0589, 2013, https://doi.org/10.4271/2013-01-0589.

[6] Kohout P. (2020) Cam design for variable valve lift system with switchable roller finger follower, Conference paper at 51st International Scientific Conference of Czech and Slovak University Departments and Institutions Dealing With the Research of Internal Combustion Engines, "KOKA 20", CTU in Prague, Czech Republic, pp. 138–148. ISBN 978-80-01-06744-4

[7] Qianfan X., Diesel Engine System Design – 1st edition, Woodhead Publishing, 2011, ISBN-13: 978-1845697150

[8] Nicholas M. P., TAKASHI M., WONJOON CH., Shape Interrogation for Computer Aided Design and Manufacturing, https://web.mit.edu/hyperbook/Patrikalakis-Maekawa-Cho/node17.html

[9] GT-Suite v2019 user manual, Gamma Technologies, LLC.

SYMBOLS AND ACRONYMS

CA	crank angle
CAE	computer aided engineering
CP	crossover point
CSW	critical shifting window
iEGR	internal exhaust gas recirculation
MLC	mechanical lash at cam
MLL	mechanical lash at latching pin
OEM	original equipment manufacturer
SRFF	switchable roller finger follower
VVA	variable valve actuation
VVL	variable valve lift
VVT	variable valve timing
$v_{diff@CP1}$	relative velocity difference at CP1
$v_{diff@CP2}$	relative velocity difference at CP2
$v_{inner}(\gamma_{CP1})$	velocity on inner cam lobe at contact point during CP1
$v_{inner}(\gamma_{CP2})$	velocity on inner cam lobe at contact point during CP2
$v_{inner}(\beta_{CP1})$	velocity on outer cam lobe at contact point during CP1
$v_{inner}(\beta_{CP2})$	velocity on outer cam lobe at contact point during CP2
α	rotation angle of camshaft from initial state
β	angle between cam profile first point and contact point at outer cam profile
γ	angle between cam profile first point and contact point at inner cam profile

SUBSCRIPTION INFORMATION FOR YEAR 2020

MECCA IS PUBLISHED THREE TIMES A YEAR

* Middle European countries profit special price ..... 200 CZK
  (in Czech crowns) without shipping costs per issue.
* Price for rest of world .....15 €
  per issue without shipping costs.
* Price for annual subscription including shipping costs for Czech republic ..... 760 CZK
* Price for annual subscription including shipping costs for other middle European countries..... 860 CZK
* Price for annual subscription including shipping costs for the rest of Europe .....56 €
* Price for annual subscription including shipping costs for the overseas.....60 €

PLEASE PAY THE AMOUNT ON THE FOLLOWING BANK ACCOUNT:

Name of account:	CVUT V PRAZE – FAKULTA STROJNI
Address of account owner:	Technická 4 16607 Praha 6 Czech Republic
Account number:	27-4095990227
Bank code:	0100
Bank address:	Komerční banka a.s., Praha 6 Dejvická 52 160 59 Praha 6 Czech Republic
Variable symbol:	241

FOR ALL QUESTIONS, PLEASE, CONTACT THE EDITOR:

Gabriela Achtenová
Czech Technical University in Prague
Technická 4, 166 07 Praha 6
Czech Republic
Tel.: +420 2 24 35 24 99, Fax: +420 2 24 35 25 00
mecca@fs.cvut.cz
gabriela.achtenova@fs.cvut.cz

LIST OF COUNTRIES PROFITTING THE SPECIAL PRICE OF MECCA:

Czech Republic, Slovakia, Poland, Hungary, Romania, Bulgaria, Former USSR republics, Former Yugoslav republics

10.14311/mecdc.2021.01.02

RANGE EXTENDER ICE MULTI-PARAMETRIC MULTI-OBJECTIVE OPTIMIZATION

MIKULÁŠ ADÁMEK
CTU in Prague, Faculty of Mechanical Engineering; Technická 4, Praha 6, 166 07, Czech Republic; E-mail: mikulas.adamek@fs.cvut.cz
RASTISLAV TOMAN
CTU in Prague, Faculty of Mechanical Engineering; Technická 4, Praha 6, 166 07, Czech Republic; E-mail: rastislav.toman@fs.cvut.cz

ABSTRACT
Range Extended Electric Vehicles (REEV) are still one of the suitable concepts for modern sustainable low emission vehicles. REEV is equipped with a small and lightweight unit, comprised usually of an internal combustion engine with an electric generator, and has thus the technical potential to overcome the main limitations of a pure electric vehicle – range anxiety, overall driving range, heating, and air-conditioning demands – using smaller battery: saving money, and raw materials. Even though several REx ICE concepts were designed in past, most of the available studies lack more complex design and optimization approach, not exploiting the advantageous single point operation of these engines. Resulting engine designs are usually rather conservative, not optimized for the best efficiency. This paper presents a multi-parametric and multi-objective optimization approach, that is applied on a REx ICE. Our optimization toolchain combines a parametric GT-Suite ICE simulation model, modeFRONTIER optimization software with various optimization strategies, and a parametric CAD model, that first provides some simulation model inputs, and second also serves for the final designs' feasibility check.
The chosen ICE concept is a 90 degrees V-twin engine, four-stroke, spark-ignition, naturally aspirated, port injected, OHV engine. The optimization goal is to find the thermodynamic optima for three different design scenarios of our concept – three different engine displacements – addressing the compactness requirement of a REx ICE. The optimization results show great fuel efficiency potential by applying our optimization methodology, following the general trends in increasing ICE efficiency, and power for a naturally aspirated concept.
KEYWORDS: RANGE EXTENDER, RANGE EXTENDED ELECTRIC VEHICLE, HYBRID ELECTRIC VEHICLE, BATTERY ELECTRIC VEHICLE, INTERNAL COMBUSTION ENGINE, SPARK-IGNITION, THERMODYNAMIC OPTIMIZATION, GENETIC ALGORITHM

SHRNUTÍ
Elektrické vozidlo s prodlouženým dojezdem (REEV) je považováno za jednu z možností, jak vyrobit cenově dostupný automobil s nízkými emisemi škodlivin a skleníkových plynů. Hlavní výhoda tohoto konceptu spočívá v malé (lehké) baterii, která by měla svojí kapacitou pokrýt většinu životního cyklu, menší baterie též snižuje cenu vozidla. Aby uživatel nebyl omezen krátkým dojezdem, je pro výjimečné případy vozidlo vybaveno tzv. prodlužovačem dojezdu. Většinou se jedná o pístový spalovací motor s generátorem, jehož pomocí se nabíjí hlavní baterie. Vývojem takového systému se zabývala řada výrobců, většina návrhů se však zakládala pouze na zkušenostech vývojářů a výsledné motory nebyly optimalizovány pro jejich provozní podmínky.
Článek pojednává o návrhu spalovacího motoru pro prodlužovač dojezdu pomocí mnoho-kriteriální a mnoho-cílová optimalizace plně parametrického termodynamického modelu, v kooperaci s CAD modelem. CAD model je použit jako zdroj vstupů pro termodynamický model a současně ke kontrole realizovatelnosti výsledků optimalizace.
Navrhovaný motor je čtyřdobý, atmosférický, dvouválec do V, s rozvodem OHV a nepřímým vstřikem paliva. Celkem jsou optimalizovány tři varianty motoru, lišící se zdvihovým objemem. Cílem je pokud možno naplnit požadavek na kompaktnost výsledného motoru.
Výsledky odpovídají trendům pro zvyšování účinnosti a výkonu spalovacích motorů a vykazují velký potenciál pro snížení spotřeby paliva spalovacího motoru.
KLÍČOVÁ SLOVA: PRODLUŽOVAČ DOJEZDU, ELEKTRICKÉ VOZIDLO S PRODLOUŽENÝM DOJEZDEM. RANGE EXTENDER, ELEKTRICKÝ AUTOMOBIL S PRODLUŽENÝM DOJEZDEM, ELEKTROMOBIL, SPALOVACÍ MOTOR, ZÁŽEHOVÝ MOTOR, TERMODYNAMICKÁ OPTIMALIZACE, GENETICKÝ ALGORITMUS

1. INTRODUCTION

Range Extended Electric Vehicles (REEV) are one of the doctrines considered for modern low emission vehicles. Main advantage of this concept comes from using the battery as small as possible, this way helping to save the rare and expensive materials used in batteries, still without causing the "range anxiety" to the user. To fully exploit this advantage and to be economically viable, the Range Extender (REx) used in REEV, needs to focus on the price, overall mass, package dimensions, and NVH (Noise Vibration and Harshness). The most common type of range extender (and the only one considered in this paper) is the internal combustion engine (ICE). Several companies have developed a REx ICE to some extent, including OEMs like Lotus, TATA, MAHLE, and some others [1; 2; 3; 4; 5].

Design concepts from table 1 suggest, that most of REx ICEs are designed primarily to fulfil the already mentioned requirements. Most of the companies try to keep the price as low as possible, which means sticking to traditional concepts of natural aspiration, indirect injection, and two valves per cylinder heads: the only major difference is AVL with its rotary REx concept [5]. All the evaluated Range Extender engines operate at stoichiometric conditions, allowing for the use of three-way catalyst to fulfill the emission regulation. Although most of the engine concepts were designed from scratch, TATA being the only difference [3], all the designs are mostly based on engineering teams' experience, and internal OEM's empirical tools, and correlations.

Literature indicates that the efficiency is subject to other parameters (especially to price). This way, the entire system's efficiency will always be poor, due to the double tank-to-wheel energy conversion. Nevertheless, the fuel consumption can be significantly reduced (which is always a positive attribute) by the engine optimization for its specific operation, even with "the cheapest" possible setup.

1.1 DESCRIPTION OF THE GENERAL IDEA

Our general idea is based on building a detailed fully parametric thermodynamic model of an ICE, equipped with simulation sub-models with appropriate predictive capabilities, and then running a multi-parametric, multi-objective optimization. The optimization result is then checked for its feasibility, using a parametric CAD model of the engine block. This not only provides a necessary engineering feedback, but also helps to capture some important trends, that can occur when changing the basic engine parameters automatically: in our study it is for instance the con-rod elongation when decreasing the bore/stroke ratio $R_{B/S}$ leading to the crank-train enlargement.

Range Extender engines are designed to provide a specific power output P_e (generally enough for the vehicle to achieve the highway speed), usually around 30 kW. The engine is expected to provide this power output at wide-open throttle conditions and for most of its lifetime. This single operating point feature makes the REx engines well suitable for a multi-parametric thermodynamic optimization mentioned above, although the general method can be easily extended on more operating points, and therefore other ICE concepts.

1.2 GOALS OF THE PAPER

Our department at Czech Technical University in Prague (CTU) has gathered vast amount of experience on ICE design optimization throughout several former projects [6; 7]. The main goal of this article is to describe an ICE design and optimization method, that combines CAE simulation tools with CAD structural design. The CAD model sets up the simulation input data, and subsequently checks the final design for its feasibility.

	AVL	MAHLE	TATA	Lotus	KSPG	AVL	
Engine configuration	I2	I2	I2	I3	V2 (90 deg)	Rotary (single)	[-]
Valvetrain layout	SOHC	SOHC	SOHC	SOHC	OHV	-	[-]
Valves per cylinder	2	2	2	2	2	-	[-]
ICE displacement V_d	0.570	0.900	0.624	1.193	0.799	0.254	[L]
Bore B	70.0	83.0	73.5	75.0	80.0	-	[mm]
Stroke S	74.0	83.0	73.5	90.0	79.5	-	[mm]
Bore/Stroke ratio $R_{B/S}$	0.946	1.000	1.000	0.833	1.006	-	[-]
Compression ratio r_c	11	10	10.3	10	N/A		[-]
ICE speed n_{ICE}	5000	4000	5500	3500	4500	5000	[RPM]
Mean piston speed c_s	12.333	11.065	N/A	10.500	11.925		[m/s]
Brake power P_e	18	30	28	36.8	30	15	[kW]
BSFC	250	250	N/A	241	N/A	260	[g/kWh]

TABLE 1: Overview of Range Extender ICE concepts
TABULKA 1: Přehled uspořádání motorů pro Range Extender

The article is divided into six chapters, that cover all the important aspects of our method, starting with the engine concept selection (in chapter 2); followed by the introduction of the thermodynamic model with its predictive sub-models, and preliminary design analysis in chapter 3. Chapter 4 then discusses the optimization setup, results, and design analyses. Chapter 5 presents some potential future developments of our methodology, and finally, chapter 6 contains important conclusions from our study.

2. ICE DESIGN CONCEPT

Choosing the right base concept is extremely important, since it has a strong direct influence on NVH, package, mass, and price. Our concept selection consists of weighing the four criteria (the lower the score, the better) in table 2, for four ICE concepts. Price is the most important parameter (weight of 4), followed by the NVH, mass, and total package: input weighing data for the package, mass, and price were taken directly from a table prepared by Mahle in [8].

The inline two-cylinder engine without balance shaft is a baseline concept; the other assessed two-cylinder designs are the I2 with balance shaft, V-twin engine (V2) with 90 degrees between the cylinder axes, and a two-cylinder with opposed pistons – Boxer engine.

The NVH data in table 2 are our GT-Suite simulation results of each assessed crank-train configuration. We obtained the simulation inputs from parametric CAD model: each engine setup had equal bore, stroke, and conn-rod lengths. First, all variants were first order statically balanced. The I2 engines were simulated for the three feasible ignition orders (0–360 degrees, 0–180 degrees, and 0–450 degrees), and the best one of these is the I2 baseline in the final table 2 comparisons (thus achieving 100%). The NVH relative value then represents a fraction of imbalanced force between the tested concept and I2 baseline. To enable the averaging of unbalanced forces and unbalanced moments together, the moments are weighted by the estimated bearing spacing. Finally, table 2 suggests, that V2 concept seems to be the most promising for REx ICE, and it is therefore chosen for our subsequent studies.

	Package	Mass	Price	NVH	Weighted average
Parameter weight	1	2	4	3	---
I2 without balance shaft	100	100	100	100	100
I2 with balance shaft	100	115	110	31.1	86.3
V2 with 90° angle	128	105	102	32.7	84.4
Boxer	104	108	103	44.7	86.6

TABLE 2: Decision table for the ICE concept selection
TABULKA 2: Rozhodovací tabulka pro výběr konceptu motoru

To sum-up our ICE design concept: later chapters of this article will deal with the optimizations of four stroke, V2, naturally aspirated, spark ignition engine with port fuel injection, and two valves per cylinder (OHV).

3. THERMODYNAMIC MODEL

A fully parametric thermodynamic model of our final design concept serves for the subsequent multi-parametric and multi-objective optimizations. The simulation model of the REx ICE was built within the 0D/1D GT-Suite simulation platform, which allows for the simulation of a whole engine thermodynamic cycle. The engine is a virtual one, with a special attention placed on the use of suitable sub-models with predictive abilities. A sub-model without a proper predictive ability could mislead the optimization and guide it to unrealistic results.

3.1 MAIN ENGINE GEOMETRY

The main parameters of the thermodynamic model are the cylinder bore B, engine operating speed n_{ICE}, and bore/stroke ratio $R_{B/S}$.

Valve design parameters are linked to the cylinder bore diameter, using empirical formulas from [9]:

- intake valve diameter $D_{v_{in}} = 0.36B$; maximum intake valve lift $L_{v_{in}} = 0.3D_{v_{in}}$;
- exhaust valve $D_{v_{ex}} = 0.3B$; maximum exhaust valve lift $L_{v_{ex}} = 0.3D_{v_{ex}}$.

The 1D intake and exhaust air paths are also fully parametric, sized accordingly to the cylinder bore B, using generic flow coefficients. Intake air path contains also an air filter, throttle, and intake manifold volume. Exhaust path then contains a simplified model of a catalyst brick, to get a realistic exhaust back-pressure.

3.2 FRICTION SUB-MODEL

Friction model has a key influence on the resulting ICE's setup, mainly on the $R_{B/S}$ ratio, and ICE operating speed. A simple *Chen-Flynn* model which was used in previous research studies showed major flaws when used in a multi-parametric optimization due to its lack of predictive ability [7]. Therefore, we applied CTU in-house friction model *Vyvaž*, created by Macek et al. [10]. In fact, its implementation into GT-Suite thermodynamic model as a sub-assembly.

This friction sub-model has three main parts: pressure part, mechanic part, and friction part. Pressure part consists of series of pipe objects, that simulate engine blow-by, and predict the pressure differences between the piston rings – essential for the piston ring and skirt friction forces calculation. Second – mechanic part, consists of detailed mechanical model of crank-train, and determines all velocities, accelerations, and forces acting on each

crank-train member. The last – friction part, calculates friction powers, FMEPs, and friction forces for each member of crank--train, and piston assembly (crank bearings, main bearings, piston pin, piston skirt, and piston rings), using results obtained from the respective mechanic and pressure parts. Friction coefficients necessary for finding the friction forces are calculated using a simple model based on a mathematical description of Stribeck curve, that expresses a friction coefficient's dependence on load, speed, and oil viscosity. *Vyvaž* model also contains empiric relations for oil, and fuel pump losses. Finally, the friction loss in valve train is calculated by Bishop's formula [9].

3.3 COMBUSTION SUB-MODEL

Another key area in spark-ignition ICE optimization is the simulation of SI combustion. We decided to use predictive phenomenological combustion model called *EngCylCombSITurb* (*SITurb*) available in GT-Suite. *SITurb* model calculates a differential equation for entrained mass rate of unburned gas with its main equation 1, where ρ_u are unburned mixture density, and A_f a flame area. S_L and S_T then represent the laminar and turbulent flame speeds.

$$\frac{dM_e}{dt} = \rho_u A_f (S_L + S_T) \tag{1}$$

These two flame speed parameters – S_L and S_T – limit the flame kernel development: during the initial phases, when the kernel size is still small, the entrainment rate is limited by the laminar flame speed S_L (equation 2); equation 3 then accounts for the flame transition into a turbulent one, with u' representing the mean fluctuating turbulent velocity, R_f the flame radius, and L_t the turbulent length scale.

$$S_L = \left[B_m + B_\phi(\phi - \phi_m)^2\right] \cdot \left(\frac{T_u}{T_0}\right)^{\alpha} \cdot \left(\frac{p}{p_0}\right)^{\beta} \cdot (1 - 2{,}06 Dil^{0.77DEM}) \tag{2}$$

$$S_T = C_s u' \left(1 - \frac{1}{1 + C_k\left({R_f}^2 / {L_t}^2\right)}\right) \tag{3}$$

SITurb needs a priori information about the turbulent flow in combustion chamber (L_t and u' parameters from equation 3). The source of these quantities is another GT-Suite's sub-model – *EngCylFlow* (*Flow*) – a *K-k-ε* kinetic energy cascade flow model, that predicts the in-cylinder charge motion and turbulence. More details on both *SITurb* and *Flow* models, their evolution, and calibration can be found in [11; 12; 13].

SITurb uses five different calibration parameters, four from equations 2 and 3 (*DEM*, C_k, C_S, and L_t), and Taylor length scale multiplier C_λ (present in the burnup rate equation dM_b/dt, as a multiplier for the Taylor microscale of turbulence). *Flow* then has its own set of four calibration parameters. So, in total we have nine calibration parameters.

First, we performed a thorough sensitivity analysis on these nine total calibration parameters, comparing the combustion model (combination of *SITurb* and *Flow*) responses on ICE geometry, ICE operating conditions (load, speed, and cooled EGR content). The sensitivity analysis showed that the burn durations vary in accordance with our general experience: however general burn rates are lower, and the overall sensitivity on operating conditions is higher (load, speed, cooled EGR).

After the sensitivity analysis we performed a calibration of the nine *SITurb* and *Flow* calibration parameters using an available set of measurement data with ICE load/speed dependencies. The set of these nine calibrated parameters was then used in all our subsequent REx ICE optimizations, discussed in next chapters.

3.4 IN-CYLINDER HEAT TRANSFER SUB-MODEL

Prediction of in-cylinder energy loss due to heat transfer is calculated with a combination of two models.

First, structure and surface temperatures are obtained with a predictive finite element (FE) GT-Suite sub-model *EngCylTWallSoln*. FE model requires a simplified geometry of all the surfaces, together with coolant and oil boundary conditions. The cylinder structure geometry is also parametric and linked to the engine main geometry.

Second, the heat transfer coefficient is determined using classical Woschni correlation without swirl [14]. This approach was successfully used in some previous CTU research projects on ICE multi-parametric optimization [6; 7].

3.5 KNOCK SUB-MODEL

Knock prediction is modeled using a basic GT-Suite model *EngCylKnock* (*Knock*), which is based on a standard calculation of knock induction time integral. *Knock* model obtains the induction time using a *Kinetics-Fit-Gasoline* correlation. This correlation predicts the induction time with combination of reduced iso-octane oxidation and reduced n-heptane oxidation mechanisms [15].

We did not calibrate the *Knock* model, because of the time constraints. However, our previous sensitivity studies showed, that the uncalibrated model tends to stay on the safe side in its response to ICE operating condition changes, and this we consider advantageous [16].

3.6 STRUCTURAL DESIGN ANALYSIS

There are two main reasons for the use of a parametric CAD model of our V2 engine block:

- CAD model helps us prepare some of the simulation input data for the friction model *Vyvaž*, that requires detailed knowledge of crank-train masses, and con-rod compensating moment of inertia with its coordinates.

- Subsequently, it serves for the final structural design's feasibility check – after running the multi-parametric optimizations.

There are some relations, that can be established only with this parametric CAD model, and which are important inputs for *Vyvaž* friction model – as we have already discussed. First of those relations is the relation between the piston assembly's mass and cylinder bore; the second one is the relation between the con-rod's length l and its geometry parameters; third one is the relation of con-rod ratio λ with bore/stroke ratio $R_{B/S}$, and bore diameter B in equation 4 (n and c are functions of cylinder bore; $\lambda = S/(2^{*}l)$. One can assume, that a designer would try to minimize the package volume using a con-rod as short as possible, because this is a parameter that plays a major role in determining the crank-train's size, and therefore the total engine's package volume.

$$\lambda = \left(-\sqrt{\frac{\left(R_{B/S} - 0.75\right)^2}{0.05882^2} + 1} \right) \cdot 0.0125 + n + \left(R_{B/S}c - 0.75c\right) \quad (4)$$

Figure 1 shows this relation in comparison with data acquired directly from the CAD model (marked by "REL" suffix in legend), for four different bore diameters B. Our correlation gives feasible results, and these are fed into *Vyvaž* sub-model ensuring higher optimization accuracy and results' feasibility.

Figure 2 with con-rod ratio λ dependence on $R_{B/S}$ ratio then shows, that for $R_{B/S}$ ratios under 0.5, the con-rod length grows rapidly (lower λ ratio means longer con-rod length). This Figure also clarifies how we chose the $R_{B/S}$ ratio lower/upper limits in table 3, that will be introduced in next chapter.

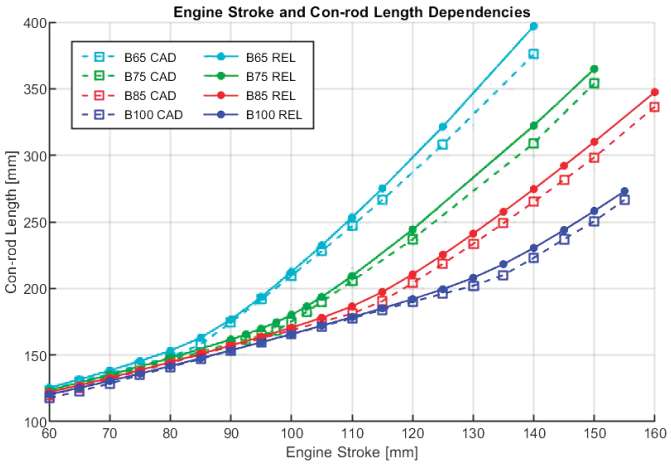

FIGURE 1: Con-rod length dependence on engine stroke (values obtained with relation 4 are marked with "REL")
OBRÁZEK 1: Délka ojnice v závislosti na zdvihu motoru („REL" značí hodnoty získané pomocí vztahu 4)

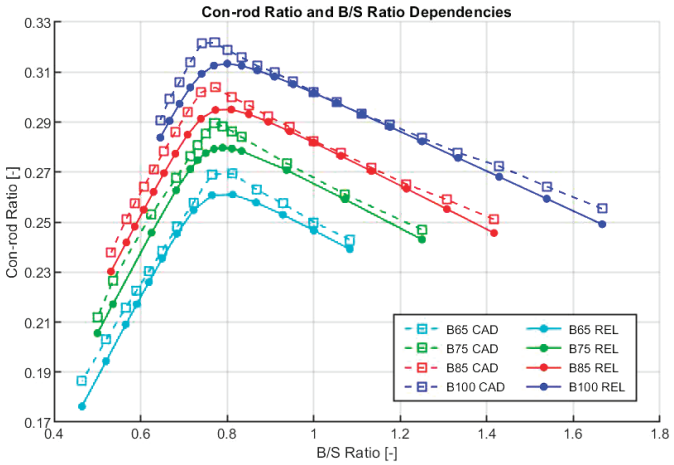

FIGURE 2: Con-rod ratio dependence on bore/stroke ratio $R_{B/S}$
OBRÁZEK 2: Závislost ojničního poměru na poměru zdvihu a vrtání $R_{B/S}$

4. OPTIMIZATION SCENARIOS

A general expectation in an optimization aimed for the best efficiency natural aspirated ICE is, that it will lead to relatively large displacement. This is however in a strong disagreement with the basic REx requirement for a compact design package, and low overall mass. To test this expectation, we decided to optimize our REx ICE model in three different scenarios, with the same P_e target of 30 kW, at the best possible BSFC. The only difference between the scenarios is the engine displacement.

In the first scenario, called V_{max}, the optimizer is not limited by the cylinder displacement, only by the minimum/maximum cylinder bore diameter B and bore/stroke ratio $R_{B/S}$. Main point of this scenario is to test, whether the optimization will properly follow the expected trends in increasing the ICE efficiency.

Second scenario V_{05} concept uses a fixed cylinder displacement of 0.5 L, hence the name. This engine's total displacement is slightly larger than most REx ICEs analyzed in chapter 1, but it is probably the most common engine displacement in automotive industry.

Last scenario is V_{035}, should represent the design's compactness requirement. Since total displacement of 0.7 L is rather small for 30 kW power output, we expect the optimized design to turn out as "sporty".

4.1 OPTIMIZATION SETUP

There are nine total parameters chosen for the optimizations, summed-up in table 3 (SA is the spark advance angle; the firing TDC represents the 0 deg CA in all angular parameters). The V_{max} scenario optimizes all of them; in the case V_{05} and V_{035} scenarios bore and stroke values are linked together because of the "locked volume", and the optimizer varies only the $R_{B/S}$ ratio.

Parameter	B [mm]	$R_{B/S}$ [-]	r_c [-]	n_{ICE} [RPM]	SA [deg CA]	IVO [deg CA]	EVC [deg CA]	F_{IVC} [-]	F_{EVO} [-]
Lower limit	60	0.5	6	1000	80	290	320	0.7	0.7
Upper limit	100	1.5	15	7000	-10	380	450	1.3	1.3
Resolution	0.1	0.005	0.1	50	1	1	1	0.004	0.004

TABLE 3: Limits and resolutions of the optimization parameters
TABULKA 3: Rozsahy a rozlišení optimalizovaných parametrů

Parameters F_{IVC} and F_{EVO} multiply the width of the base valve lift curves, and by that control the inlet valve opening event or exhaust valve closing events respectively (Note: unity values of F_{IVC} and F_{EVO} correspond to 210 deg CA from open to closed valve, at 1 mm lift).

All the optimizations are run using modeFRONTIER's *pilOPT* hybrid algorithm, that combines local and global search, and is recommended for multi-objective problems [17]. *pilOPT* algorithm is then searching for the thermodynamic optima, trying to fulfill also the P_e demand. Each scenario optimization took about 10 000 design iterations.

As we have already discussed in our introductory part, we use a fully parametric CAD model of V2 engine block for the design feasibility check, since a thermodynamically optimal design is not necessarily also feasible from the structural design viewpoint.

	V_{max}	V_{05}	V_{035}	
B^*	99.50	98.15	75.74	[mm]
$R_{B/S}^*$	0.735	1.485	0.975	[-]
n_{ICE}^*	2150	3200	4650	[RPM]
r_c^*	14.2	12.7	14.1	[-]
SA^*	22.0	36.0	27.0	[deg CA]
S^*	135.37	66.09	77.68	[mm]
V_d	2.11	1.00	0.70	[L]
C_S	9.70	7.05	12.04	[m/s]
BSFC	214.0	229.8	238.5	[g/kWh]
BMEP	7.95	11.25	11.07	[bar]
η_v	58.67	89.27	91.08	[%]
η_m	92.78	90.70	84.48	[%]

TABLE 4: Results for all three optimization scenarios
TABULKA 4: Výslední hodnoty pro všechny optimalizační scénáře

4.2 OPTIMIZATION RESULTS

Since the optimization is multi-objective, optimal results are received in a Pareto front, which is a set of optimal values, where achieving improvement in one of the objectives will worsen the other. In our case, designs with lower BSFC tend to be further away from the desired power output, and vice versa. The optimal designs were then selected from the Pareto front using standard criterial function F (equation 5), where the weight coefficient for BSFC (α_{i1}) is 0.9, and for brake power P_e (α_{i2}) it is 0.1. The fraction $X_i/X_{i,\,max}$ in equation 5 represents a normalization of Pareto front values, so that the two different objective functions X_i can be combined into one equation; $X_{i,\,max}$ is the maximum value of the ith objective function in Pareto set.

$$F = \sum_{i=1}^{k} \alpha_i \frac{X_i}{X_{i,max}} \tag{5}$$

4.2.1 OVERALL RESULTS

Results of all three optimization scenarios are summarized in table 4 and Figure 3. While table 4 contains the set of optimal (independent – labelled with '*') parameters, main thermodynamic outputs, and some dependent parameters; Figure 3 then shows the comparison of valve lift curves for each scenario.

The V_{max} scenario engine turned out as the most efficient, with the best BSFC value of 214 g/kWh. But it is also the largest of the three engines. The final V_{max} volume is 2.1 L, with a long stroke $R_{B/S}$ of 0.735, leading to a mean piston speed of 9.70 m/s. Large volume means that the engine was able to achieve demanded P_e with only 2150 RPM – following the ICE down-speeding trend. A look at the Figure 3 shows, that the V_{max} engine uses inlet valve open for extremely short time, running in Miller cycle.

Tendency to push towards Miller cycle is well known. However, in comparison to similar previous optimizations [7], the optimizer was given bigger freedom in valve timing parameters, resulting in "stronger" Miller cycle. The combination of large volume, low speed, and Miller cycle leads to rather small BMEP of 7.95 bar, and volumetric efficiency of only 58.7 %. Although such REx engine would hardly fulfil package requirement, lower BMEP engines tend to be robust and reliable, which might be useful for an ICE operating at WOT right after start-up.

V_{max} concept also has relatively large compression ratio of 14.2. This can seem extreme, but in combination with spark advance of 22 deg CA BTDC, and Miller cycle especially, it is feasible.

The V_{05} scenario achieves worse BSFC results compared to the V_{max} variant, with a short stroke $R_{B/S}$ ratio of 1.485, at higher operating speed 3200 RPM, but lower c_s of 7.05 m/s. We have

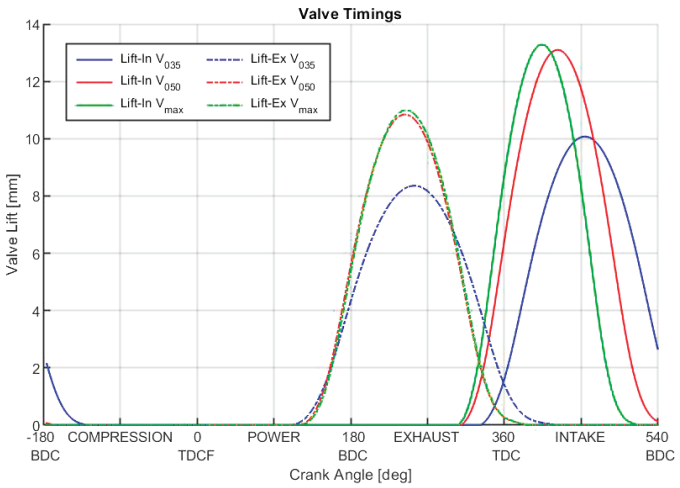

FIGURE 3: Valve lift curves of optimized engines
OBRÁZEK 3: Ventilové zdvihové křivky optimalizovaných motorů

seen some similar behavior before e.g. in [7], but there it was caused probably by the simple *Chen-Flynn* friction model [9], that lacks the predictive abilities, and therefore preferred this short-stroke configuration. In this case, however, we think it is because of achieving good volumetric efficiency, due to the direct link between the bore size and inlet valves diameter. The fact that V_{05} engine achieves high BMEP of 11.25 bar despite using some level of Millerization supports our assumption. Compression ratio is 12.7 which is lower than in the previous V_{max} scenario, due to the short stroke configuration, that leads to the increased knock tendencies [1]. However, with such a short stroke, even this compression ratio might be technically challenging to achieve.

The last V_{035} scenario was chosen with rather small volume for such power output; the engine BSFC, ICE operating speed, and mean piston speed grow accordingly. The optimal $R_{B/S}$ ratio is also a bit surprising, since the engine is slightly long stroke. The reason for this is probably the tendency of *Vyvaž* friction model (according to its author) to overrate the piston skirt friction growing with engine bore. Another parallel explanation is that Bishop's formula uses the ICE operating speed and valve diameter to determine the valvetrain losses: since the valve diameter is linked directly to the engine bore, smaller bore actually leads to relatively high mechanical efficiency of 84.5 %, despite high RPMs and mean piston speed (4650 RPM, 12.04 m/s). Yet, the small inlet valve area, pushes the optimizer to change the valve timing approach, compared to the first two scenarios: V_{035} engine uses a later IVC angle compared to other scenarios. This way the engine achieves sufficient cylinder filling, although with slight backflow just before IVC, reducing effective compression ratio thus improving knock robustness.

4.4.2 PACKAGE COMPARISON

From the package standpoint, all three design scenarios were also compared using parametric CAD model of V2 engine block, since comparing just their volume is not particularly accurate, because the engine size is strongly influenced by $R_{B/S}$ ratio, and con-rod length (Figure 4, and table 5). Table 5 also contains estimated masses of the main engine components.

The V_{max} engine is by far the largest of the three – as expected. It is rather interesting, that the two other scenarios V_{05} and V_{035} are very similar from the package standpoint, though V_{035} is slightly shorter. According to our CAD model, all designs are

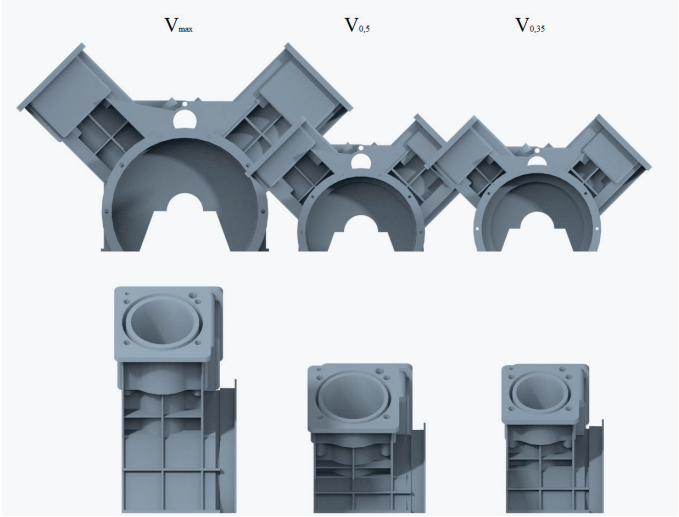

FIGURE 4: Engine block CAD models (from left V_{max}, V_{05}, V_{035})
OBRÁZEK 4: CAD modely bloků (zleva V_{max}, V_{05}, V_{035})

	Width [mm]	Height [mm]	Length [mm]	Block Mass [kg]	Piston assembly Mass [kg]	Con-rod Mass [kg]	Con-rod Length [mm]
V_{max}	574.8	356.1	192.3	13,15	0,73	0,70	219,9
V_{05}	401.2	231.8	186.6	6,58	0,71	0,54	126,7
V_{035}	389.4	232.5	160.9	5,88	0,36	0,57	144,5

TABLE 5: Engine blocks' dimensions and estimated components' masses
TABULKA 5: Rozměry bloků motorů a odhadnuté hmotnosti hlavních komponent

feasible; however, V_{05} variant is on the limit, and some of the design features would be a very tight fit.

5. POTENTIAL FOR FUTURE DEVELOPMENT OF THE OPTIMIZATION METHODOLOGY

The designs resulting from our optimizations are generally feasible and achieve high yet not unrealistic efficiencies for OHV designs. Despite these positive results, there is still some further potential in the development of our optimization methodology, especially from the viewpoint of the structural design, specifically in two areas.

The first area is referenced to the fact, that we do not scale the main and conn-rod bearing diameters with bore size. And these are important inputs for *Vyvaž* friction model. A change in the con-rod bearing diameter would also influence the relation developed for con-rod ratio calculation (equation 4). We have already prepared some possible corrections to this formula, but these will be applied together with the bearing size scaling.

The second area is connected to the valve lift scaling. Currently we use a scaling coefficient F_v for the respective intake/exhaust lift vectors (equation 6, where L_v is the valve lift and D_v the valve diameter) based on Heywood's formula, first introduced in chapter 3.1 on main engine geometry.

$$0.3 \leq \frac{L_v}{D_v} => F_v = 0.3\frac{D_v}{L_v} \tag{6}$$

This simple relation gives decent result from the thermodynamic perspective. Further increase in the intake valve lift from the optimal value of the V_{max} design has a small additional positive effect on BSFC, which is clear from Figure 5.

In practice, the lift curve is usually limited by the valve train dynamics. Valve acceleration is determined by the lift curve shape – this acceleration relation can be simplified to just valve lift and engine speed. However, REx ICE operates only in one primary operating point and it is not controlled by the driver: this means, that there is little chance of over-speeding the engine. The lift curves can be therefore designed exactly for this one operating point, even possibly saving some extra fuel.

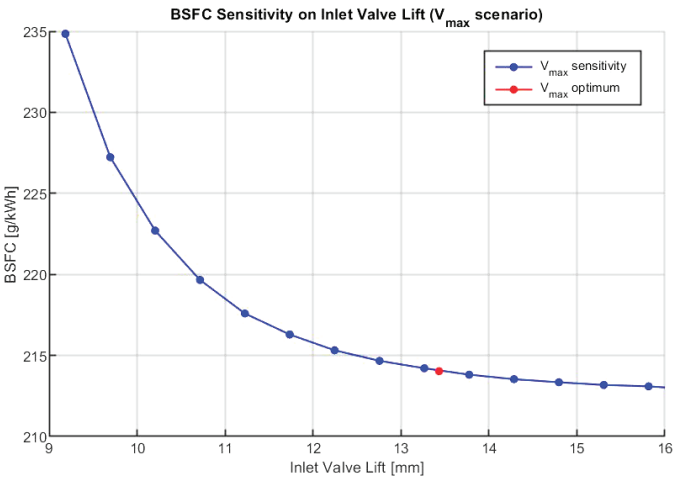

FIGURE 5: BSFC dependence on the inlet valve lift for V_{max} scenario
OBRÁZEK 5: Závislost měrné spotřeby na zdvihu sacího ventilu pro scénář V_{max}

6. CONCLUSION

Our paper presents a multi-parametric, multi-objective design optimization methodology, that was tested on a case of three design scenarios for a four-stroke, V-twin, natural aspirated, spark-ignition REx ICE, operating in a single point REEV's operation.

We defined our REx engine concept, aiming at the best possible balance of achievable mass, package, overall design simplicity and therefore low cost, based on the literature research and using a design selection table. The other layouts that we considered were inline two-cylinder variants with or without balance shaft, and an opposed pistons engine – Boxer.

Thermodynamic 0D/1D model was built within the GT-Suite simulation environment, with a special emphasis on predictive ability of its sub-models. Our paper briefly discusses some of these sub-models: CTU in Prague in-house built friction model, GT-Suite's phenomenological predictive SI combustion model, knock model, and finally the in-cylinder heat transfer model.

Apart from the GT-Suite simulation model, our methodology uses also a parametric CAD model of the engine block. This CAD model provides some important input data for the GT-Suite sub--models to enhance the optimization accuracy, and it is also used for the optimization result structural design's feasibility check.

Finally, the multi-parametric and multi-objective optimizations of three different design scenarios featuring different engine displacement with the same power output goal were carried out in a modeFRONTIER optimization platform, using a hybrid algorithm *pilOPT*. Resulting REx ICE designs are realistic, following the current trends of ICE efficiency increase (Millerization and down-speeding) and power increase for natural aspirated engine.

Our future work will mainly focus on further enhancements of our optimization methodology, adding more details of the crank--train mechanism design into the simulation sub-models. Future simulation studies will consider different engine layouts.

ACKNOWLEDGEMENTS

This work was realized using support of:

- Technological Agency, Czech Republic, programme National Competence Centres, project # TN01000026 Josef Bozek National Center of Competence for Surface Vehicles.

- The Grant Agency of the Czech Technical University in Prague, grant No. SGS19/104/OHK2/2T/12.

This support is gratefully acknowledged.

LIST OF ABBREVIATIONS

BTDC	Bottom Top Dead Center
CAD	Computer Aided Design
CAE	Computer Aided Engineering
CTU	Czech Technical University in Prague
EGR	Exhaust Gas Recirculation
FE	Finite Element
I2	Inline two-cylinder Engine
I3	Inline three-cylinder Engine
ICE	Internal Combustion Engine
NVH	Noise Vibration and Harshness
OEM	Original Equipment Manufacturer
OHV	Over Head Valve
REEV Range	Extended Electric Vehicle
REx	Range Extender
SI	Spark Ignition
SOHC	Single Over Head Camshaft
TDC	Top Dead Center
V2	V-twin Engine
WOT	Wide Open Throttle
FMEP	Friction mean effective pressure
BMEP	Brake mean effective pressure
BSFC	Brake-specific fuel consumption
CA	Crank angle

LIST OF SYMBOLS

A_f	Flame area
B_m	Maximum laminar speed
$B\phi$	Laminar speed roll-of value
C_K	Flame kernel growth multiplier
C_S	Turbulent flame speed multiplier
C_λ	Taylor length scale multiplier
$D_{v_{ex}}$	Exhaust valve diameter
$D_{v_{in}}$	Intake valve diameter
F_v	Valve lift scaling coefficient
$L_{v_{ex}}$	Maximum exhaust valve lift
$L_{v_{in}}$	Maximum intake valve lift
L_t	Turbulent length scale
M_b	Burnup mass
M_e	Entrained mass
P_e	ICE brake power
$R_{B/S}$	Bore/stroke ratio
R_f	Flame radius
S_L	Laminar flame speed
S_T	Turbulent flame speeds
V_d	ICE displacement
$X_{k,max}$	Pareto set's maximum value of the objective function
X_k	Optimization objective function
C_s	Mean piston speed
n_{ICE}	Engine speed
p_0	Reference pressure
r_c	Compression ratio
α_k	Criterial function weight coefficient
η_m	Mechanical efficiency
η_v	Volumetric efficiency
ρ_u	Density of unburned gas
ϕ_m	Fuel/air equivalence ratio at maximum laminar flame speed
B	Bore
DEM	Dilution exponent multiplier
Dil	Mass fraction of the residuals in the unburned zone
F	Criterial function
S	Stroke
SA	Spark advance angle
c	Con-rod ratio relation coefficient 1
n	Con-rod ratio relation coefficient 2
p	Pressure
u'	Mean fluctuating turbulent velocity
β	Pressure exponent
λ	Con-rod ratio
ϕ	Fuel/air equivalence ratio

REFERENCES

[1] Turner J, Blake D, Moore J, et al. (2010) The Lotus Range Extender Engine. SAE International 2010-01-2208:34. https://doi.org/10.4271/2010-01-2208

[2] Andert J, Kohler E, Niehues J, Schurmann G (2012) KSPG RANGE EXTENDER: A NEW PATHFINDER TO ELECTROMOBILITY. MTZ WORLDWIDE 2012:7. https://doi.org/10.1007/s38313-012-0170-1

[3] Agarwal A, Lewis A, Akehurst S, et al. Development of a Low Cost Production Automotive Engine for Range Extender Application for Electric Vehicles. SAE International 2016-01-1055. https://doi.org/10.4271/2016-01-1055

[4] Atzwanger M, Hubmann C, Schoeffmann W, et al. Two-Cylinder Gasoline Engine Concept for Highly Integrated Range Extender and Hybrid Powertrain Applications. SAE International 2010-09-28. https://doi.org/10.4271/2010-32-0130

[5] Fraidl GK, Fisher R, Hubmann C, et al. (2009) Range Extender Module: Enabler for Electric Mobility. ATZautotechnology 2009:40–49. https://doi.org/10.1007/BF03247140

[6] Bogomolov S, Dolecek V, Macek J, et al. (2014) Combining Thermodynamics and Design Optimization for Finding ICE Downsizing Limits: 2014-04-01. SAE International 2014. https://doi.org/10.4271/2014-01-1098
[7] Toman R, Brankov I (2018) Multi-Parametric and Multi-Objective Thermodynamic Optimization of a Spark-Ignition Range Extender Ice. Sciendo 2018:459–466. https://doi.org/0.5604/01.3001.0012.4368
[8] Bassett M, Thatcher I, Bisordi A, et al. Design of a Dedicated Range Extender Engine. SAE International 2011-01-0862. https://doi.org/10.4271/2011-01-0862
[9] HEYWOOD, John. Internal combustion engine fundamentals. 1. New York: McGraw-Hill, 1988. ISBN 978-0070286375.
[10] Macek J, Fuente D, Emrich M (2011) A Simple Physical Model of ICE Mechanical Losses. SAE International 2011-01-0610. https://doi.org/10.4271/2011-01-0610
[11] Mirzaeian M, Millo F, Rolando L (2016) Assessment of the Predictive Capabilities of a Combustion Model for a Modern Downsized Turbocharged SI Engine. SAE International 2016-01-0557. https://doi.org/10.4271/2016-01-0557
[12] Rastislav T, Jan M (2017) Evaluation of the Predictive Capabilities of a Phenomenological Combustion Model for Natural Gas SI Engine. Journal of Middle European Construction and Design of Cars: The Journal of Czech Technical University 2017:37–48. https://doi.org/10.1515/MECDC20170007
[13] Fogla N, Bybee M, Mirzaeian M, et al. (2017) Development of a K-k-ε Phenomenological Model to Predict In--Cylinder Turbulence. SAE International Journal of Engines 10:562–575. https://doi.org/10.4271/2017-01-0542
[14] Woschni G (1967) A Universally Applicable Equation for the Instantaneous Heat Transfer Coefficient in the Internal Combustion Engine. SAE International 670931. https://doi.org/10.4271/670931
[15] Ra Y, Reitz R (2008) A reduced chemical kinetic model for IC engine combustion simulations with primary reference fuels. ScienceDirect 2008:713–738. https://doi.org/10.1016/j.combustflame.2008.05.002
[16] Adámek M (2020) OPTIMALIZACE TERMODYNAMIKY A KONSTRUKCE SPALOVACÍHO MOTORU PRO RANGE EXTENDER. Diplomová práce
[17] ModeFrontier User Guide: Release 2018R3, 2018 ed.. ESTECO

Received for publication in 2018 10.14311/mecdc.2021.01.03

IN-CYLINDER FLOW CHARACTERIZATION USING VORTICITY BASED PARAMETERS

PETR HATSCHBACH, OLDŘICH VÍTEK, RADEK TICHÁNEK
Czech Technical University in Prague, Department of Automotive, Combustion Engine and Railway Engineering,
Technická 4, 16607 Prague 6, Czech Republic, Tel.: +420224352492, E-mail: petr.hatschbach@fs.cvut.cz

ABSTRACT
The paper deals with intake swirling flow characterization in the cylinder of IC engine. The commonly used method based on the swirl resp. tumble number from angular momentum flux evaluation does not need to give the appropriate values in some cases. Typically, in the case of two intake ports, a counter-rotating swirl vortex pair is presented. However their summary angular momentum flux is zero a thus corresponding swirl number is zero too. In order to correctly quantify these cases, it is proposed to evaluate so called vorticity numbers, i.e. dimensionless numbers based on vorticity evaluation. Concrete results are evaluated from data obtained using 3-D CFD simulation in AVL FIRE code. Comparison of variously defined vorticity numbers with each other and with the vortex numbers is performed. A practical way of calculating the vorticity numbers was also suggested with regard to possible adverse effects of the velocity gradients at the cylinder wall.
KEYWORDS: IN-CYLINDER FLOW, SWIRL NUMBER, TUMBLE NUMBER, VORTICITY

SHRNUTÍ
Článek se zabývá problematikou kvantifikace úrovně velkých vírových pohybů ve válci spalovacího motoru. Obvykle používaný způsob založený na vyhodnocení vírového čísla swirlu a tumblu z toku momentu hybnosti nemusí v některých případech dávat odpovídající hodnoty. Typicky v případě dvou sacích kanálů vzniká výrazná dvojice protiběžných vírů, která ale souhrnně má nulový moment hybnosti a tedy i vírové číslo. Aby bylo možné tyto případy správně kvantifikovat, je navrženo vyhodnocovat vířivostní čísla, tj. bezrozměrná čísla založená na vyhodnocení vířivosti. Konkrétní výsledky jsou dokumentovány na datech získaných pomocí 3-D CFD simulace v programu AVL FIRE. Je provedeno porovnání jednotlivých vířivostních čísel navzájem i s vírovými čísly. Byl navržen i praktický způsob výpočtu vířivostních čísel s ohledem na možné nepříznivé ovlivnění velkými rychlostními gradienty u stěny válce.
KLÍČOVÁ SLOVA: PROUDĚNÍ VE VÁLCI, VÍROVÉ ČÍSLO, VÍROVÉ ČÍSLO TEČNÉ ROTACE, VÍROVÉ ČÍSLO PŘÍČNÉ ROTACE, VÍŘIVOST

1. INTRODUCTION
Knowledge of gas motion during exchange phase of internal combustion engine (ICE) is very important for optimizing following engine cycle phases – compression and combustion. In-cylinder flow during gas exchange has a significant impact for improving engine combustion performance in terms of large-scale coherent structure formation and in-cylinder turbulence level. In-cylinder flow is very complicated dynamic process, but to make it possible to describe it by the available resources, it is necessary to make some simplifications.

The first simplification consists in the idea of two predominant shapes of the in-cylinder coherent flow structure to swirl and tumble motion – Figure 1. These basic flow structures play an important role due to their ability to maintain turbulence level during compression and enhance mixing of fuel and air.

Determination of swirling motion under conditions of actual engine operation is very demanding and expensive. Experimentally it is feasible only with test engine with optical access by using optical velocity measurement method like LDA or PIV. Full numerical simulation of real in-cylinder flow is very difficult, expensive and time consuming.

Therefore, although in-cylinder flow is a very dynamic process, the second simplification – steady flow testing of cylinder head – is a widely used method in development of engines. Steady flow testing can be done experimentally using a steady flow test rig or by means of numerical simulation.

A non-dimensional parameters called Swirl, resp. Tumble Number are used for swirl or tumble level characterization. Unfortunately no standard testing methodology currently exists.

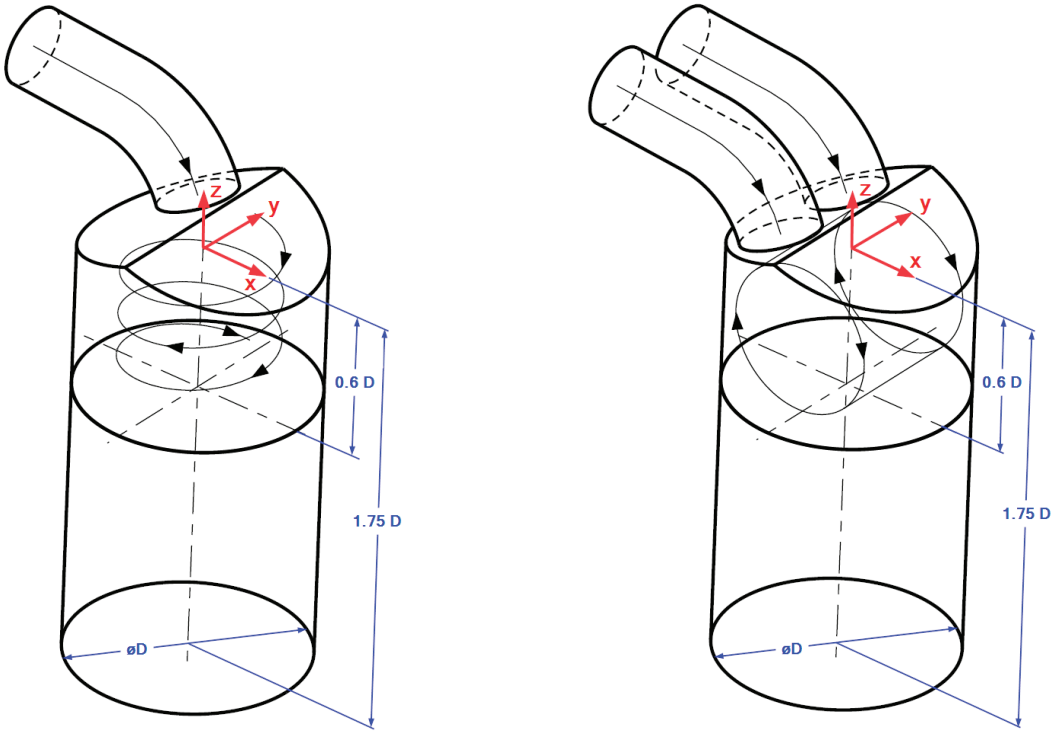

FIGURE 1: Swirl and Tumble – single opened port and both opened ports cases – coordinate systems and position evaluation planes
OBRÁZEK 2: Swirl a tumble – varianty jednoho a obou otevřených kanálů – souřadný systém a poloha vyhodnocovacích rovin

Angular momentum flux based definitions of swirl or tumble number are more commonly used. However in some cases their use may give obviously misleading results.
Therefore new non-dimensional parameters based on vorticity evaluation were proposed. Three different parameters are defined in the present article and their use is compared on two typical examples of in-cylinder flow. These examples also show that it is a very important how these parameters are evaluated.

2. ANGULAR MOMENTUM FLUX BASED PARAMETERS

In-cylinder swirling flow is most often characterized by the angular momentum of cylinder charge. During the steady flow test, you can evaluate (or measure) the angular momentum flux in some cross section area in the engine cylinder:

$$\dot{\vec{B}} = \int_A (\vec{r} \times \varrho\vec{u})\vec{u} \cdot dA \qquad (1)$$

where: ϱ ... density, $r^{\rightarrow}$... position vector, $u^{\rightarrow}$ ... velocity vector, A ... cross section area.
Displacement of the cross section corresponds to the position of the measurement element during swirl or tumble measurement. In both cases, cross section is a circular area, perpendicular to the z-axis, D ... diameter = cylinder bore. For the honeycomb torque meter used for the swirl measurement, displacement is 1.75 D (D ... diameter = cylinder bore), for tumble measurement by means original CTU tumble meter [1], displacement is 0.6 D.
Swirl is characterized by swirl- i.e. z-component of angular momentum flux $\dot{\vec{B}}$:

$$\dot{B}_S = \dot{B}_z = \int_A (x.u_y - y.u_x)\varrho u_z dA \qquad (2)$$

For tumble characterization it is necessary to merge x and y component of angular momentum flux $\dot{\vec{B}}$:

$$\dot{B}_x = \int_A y\varrho u_z^2 dA \qquad \dot{B}_y = -\int_A x\varrho u_z^2 dA \qquad (3)$$

$$\dot{B}_T = \sqrt{\dot{B}_x^2 + \dot{B}_y^2} \qquad (4)$$

Angular momentum flux components $\dot{B}_S$ and $\dot{B}_T$ can be measured or evaluated from CFD simulations. In this case, integrals must be evaluated numerically as sums.
Supposing that the cylinder charge is a solid rotating body, we can express angular momentum flux:

$$\dot{B} = \dot{I}.\omega = \dot{m}r_I^2.\omega \qquad (5)$$

where: $\dot{I}$... moment of inertia flux, ω... angular speed of solid body, $\dot{m}$... mass flow rate, r_I ... radius of gyration ($r_I^2 = D^2/8$ for circular cylinder or disc about its axis).
The angular speed of charge equivalent solid body rotation for swirl and tumble are:

$$\omega_S = \frac{8.\dot{B}_S}{\dot{m}.D^2} \qquad \omega_T = \frac{8.\dot{B}_T}{\dot{m}.D^2} \tag{6}$$

Non-dimensional swirling parameters are defined as ratio between vortex angular speed and fictitious engine angular speed ω_e. Engine angular speed can be expressed from the equation for the mean piston speed $u_{z\,mean}$ – after some modifications:

$$u_{z\,mean} = 2Zn_e \qquad u_{z\,mean} = \frac{\dot{m}}{\rho\frac{\pi D^2}{4}} \qquad \omega_e = 2\pi n_e \tag{7}$$

$$\omega_e = \frac{4.\dot{m}}{\rho.D^2.Z} \tag{8}$$

where: n_e ... crankshaft rotational speed [1/s], Z... stroke.

Rewriting the equations (6) and (8) the swirl and tumble number can be expressed as:

$$SN = \frac{\omega_S}{\omega_e} = \frac{2.Z.\rho.\dot{B}_S}{\dot{m}^2} \tag{9}$$

$$TN = \frac{\omega_T}{\omega_e} = \frac{2.Z.\rho.\dot{B}_T}{\dot{m}^2} \tag{10}$$

For better comparison of results between different engines (in terms of design), a reduced swirl and tumble numbers are defined:

$$SN_r = SN \cdot \frac{D}{Z} = \frac{2.D.\rho.\dot{B}_S}{\dot{m}^2} \tag{11}$$

$$TN_r = TN \cdot \frac{D}{Z} = \frac{2.D.\rho.\dot{B}_T}{\dot{m}^2} \tag{12}$$

This definition reduces the above-mentioned swirl and tumble numbers to the case of engine with 'square' design (bore equals stroke). Reduced numbers do not have in terms of steady test a misleading dependence on the stroke Z.

3. VORTICITY BASED PARAMETERS

Vorticity $\vec{\omega}$ describes a local value of fluid rotation in the target plane. For example, for swirl characterization is important z-component of vorticity in z=$const$ plane:

$$\omega_z = \frac{\partial u_y}{\partial x} - \frac{\partial u_x}{\partial y} \tag{13}$$

The vorticity was used to characterize in-cylinder swirling flow in works [2] [3]. In [2] the velocity and vorticity field in plane area was only qualitatively monitored, in [3] were defined equations for computing average, absolute and RMS circulations about an enclosed contour. Integral parameters average, absolute and RMS vorticity were defined in [4]. These definitions are also suitable for evaluation on irregular meshes.
Non-dimensional parameters based on vorticity evaluation were defined in [5]. But those parameters are not very well named, because terms swirl and tumble ratios are often used for non-dimensional weighted sum of the angular momentum introduced to the cylinder during the whole intake phase.
This paper defines three dimensionless parameters based on three methods of mean vorticity evaluating:

- AVG swirl vorticity number $VN_{z\,AVG}$ computed from AVG vorticity $\omega_{z\,AVG}$ calculated as area weighted mean z-component of vorticity:

$$VN_{z\,AVG} = \frac{\omega_{z\,AVG}}{2.\omega_e} \qquad \omega_{z\,AVG} = \frac{1}{A}\int_A \left(\frac{\partial u_y}{\partial x} - \frac{\partial u_x}{\partial y}\right) dA \tag{14}$$

ABS swirl vorticity number $VN_{z\,ABS}$ computed from mean vorticity $\omega_{z\,ABS}$ calculated as area weighted absoluted value z-component of vorticity:

$$VN_{z\,ABS} = \frac{\omega_{z\,ABS}}{2.\omega_e} \qquad \omega_{z\,ABS} = \frac{1}{A}\int_A \left|\frac{\partial u_y}{\partial x} - \frac{\partial u_x}{\partial y}\right| dA \tag{15}$$

RMS swirl vorticity number $VN_{z\,RMS}$ computed from mean vorticity $\omega_{z\,RMS}$ calculated as area weighted root mean square value z-component of vorticity:

$$VN_{z\,RMS} = \frac{\omega_{z\,RMS}}{2.\omega_e} \qquad \omega_{z\,RMS} = \sqrt{\frac{1}{A}\int_A \left(\frac{\partial u_y}{\partial x} - \frac{\partial u_x}{\partial y}\right)^2 dA} \tag{16}$$

Definition of AVG vorticity number corresponds to the definition of swirl or tumble ratio in [5].
ABS vorticity number can only be positive because it is calculated only from the absolute values of the partial vorticities. Each

microscopic circulation contributes positively to the total sum. It is believed that this definition could be applicable to the overall quantification e.g. two counter-rotating vortex structures.
RMS-vorticity number will be qualitative similar to ABS vorticity number, but large vorticities will have a larger weight due to the calculation with quadrate of vorticity.
For swirling flow like a rotating rigid body, vorticity ω_z in each point of $z=const$ area and mean vorticity $\omega_{z\,AVG}$ (and absoluted vorticity $\omega_{z\,ABS}$ too) have a same constant value equal to twice the angular velocity of rotating flow.

4. COMPUTED CASES AND METHOD OF EVALUATION

The results of simulations of steady flow test bench described in work [6] and other newly calculated results were used for comparison in the previous part described non-dimensional parameters. These are the results of intake port steady flow bench simulation of 4-valve SI engine (bore 76.5 mm). Two different cases were calculated: both intake valves are open (classical configuration, typical for SI engine, tumble dominated flow pattern) and single intake valve is open (unconventional, swirl dominated flow pattern). The valve lift was set from 1 to 9 mm.
Flow field was calculated by means of 3D CFD code AVL FIRE. PANS turbulence model, 4 boundary layers with 0.15 mm boundary layer thickness and unsteady simulation mode were used (up to time 0.160 s with step 0.00001 s). Boundary conditions correspond to steady flow test bench measurement setup – the most important one is the pressure difference between inlet and outlet was constant at the value of 5 kPa. More details about the calculation settings are described in [6].

Swirl and vorticity numbers were evaluated in planes placed 0.6 or 1.75 bore diameter respectively away from the cylinder head. These distances correspond to the location of the CTU tumble meter or honeycomb swirl meter. AVL FIRE command-line tool fire_utils_integrate was used to integrate CFD results over appropriate cell selection [7]. Subsequent evaluation was performed in the MS Excel spreadsheet.

5. RESULTS AND DISCUSSION

Evaluation of swirl and tumble number depending on valve lift is the usual method of large vortex movements' characterization. The case of both intake valve opened is shown in Figure 2. Tumble is dominant shape of the in-cylinder flow structure. The case of single intake valve opened is shown in Figure 3. Swirl is expected here as the main vortex shape. It is possible to make these conclusions:

- Swirl number in the case of both valve opened is practically zero. Only tumble number is evaluable.
- In the case of single valve opened it is possible to evaluate both swirl and tumble. Both swirl and tumble number curves have the similar quantity and trend.
- Relative level of large vortex structure in the case of both opened valves is always less than for single open valve case.
- Swirl number decreases slightly with the distance from the cylinder head.

Further evaluations will focus on the swirl in-cylinder motion. In Figure 4, 5, 6 and 7 are shown velocity and vorticity fields in distances 0.6D and 1.75D from cylinder head and for both cases of valve opening.

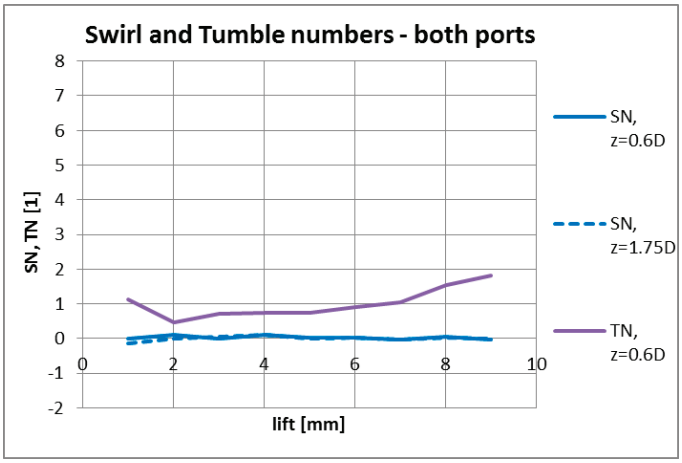

FIGURE 2: Swirl and Tumble number – dependence on valve lift – the case of both intake valves being opened.
OBRÁZEK 2: Vírová čísla swirlu a tumblu – závislost na zdvihu ventilu – varianta se dvěma otevřenými sacími ventily.

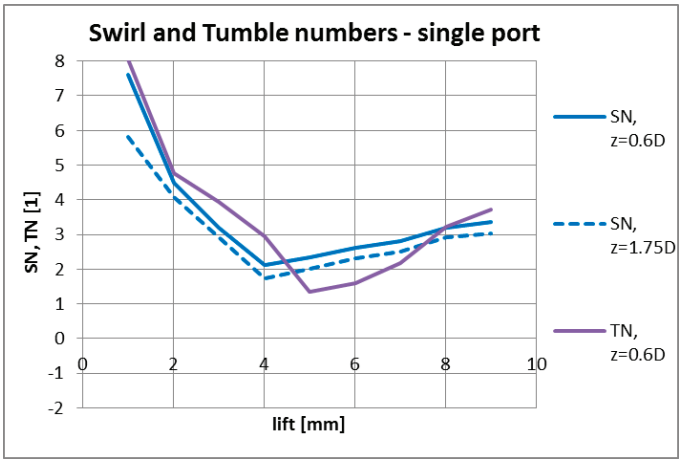

FIGURE 3: Swirl and Tumble number – dependence on valve lift – the case of single intake valve being opened.
OBRÁZEK 3: Vírová čísla swirlu a tumblu – závislost na zdvihu ventilu – varianta s jedním otevřeným sacím ventilem.

It can be seen that in the case of both valves opened – Figure 4 and 5, significant counter-rotating vortex pair is presented. However the swirl number SN, calculated from the angular momentum flux according to (9), is practically zero for all valve lift values. This is due to the fact that both swirl structures are approximately identical but counter-rotating, so that the angular momentum flux is virtually zero. Therefore, it is clear that the quantitative evaluation using the swirl number does not correspond to reality in these cases.

Because of their opposite orientation, both vortex will interact, slow down and gradually collapse into smaller vortex and chaotic turbulence in the intake stroke and early compression stroke. Just by comparing the velocity fields in distances 0.6D and 1.75D it is obvious that the vortex decay will be faster in the case of two counter-rotating vortices (both valve opened) than in case of single valve opened, when a single large vortex is created and filling the entire space of cross section. However, they certainly represent a significant part of the large vortex movements and should be considered.

A possible way to quantify the vortex level in these cases is to use appropriately defined vorticity numbers. The dependency of AVG, ABS and RMS vorticity number on valve lift is presented in Figure 8, 9 and 10 for cases of integration by formulas (14), (15) and (16) respectively. Vorticity numbers are evaluated in distances 0.6D and 1.75D and in circular area having 4 different diameters: 76.5 mm (the entire cylinder cross section), 76 mm, 74 mm and 72 mm. The case of both opened valvesi on the left, the case of single opened valve is on the right.

The first interesting conclusion follows from the chart of AVG vorticity number in Figure 8. AVG vorticity number is equal to zero when computed across the entire cross-section (D = 76.5 mm). This is in conformity with the Green's theorem, which describes a relationship between the macroscopic circulation around closed curve and the sum of all the microscopic circulation that is inside this curve. We can write integral in formula (14) as:

$$\int_A \left(\frac{\partial u_y}{\partial x} - \frac{\partial u_x}{\partial y} \right) dA = \oint_{\partial A} \vec{u} \cdot d\partial A = 0$$

and this integral is equal zero because of the zero fluid velocity $\vec{u}$ at the wall.

The second conclusion follows from Figure 8 left. For case of both intake ports opened the AVG vorticity number oscillates around zero. Therefore AVG vorticity number is not able to capture the effect of two counter-rotating vortices – like classical swirl number computed from angular momentum flux

The third note is concerning the method of practical evaluation of the vorticity number. In the practical evaluation of the vorticity numbers, it is necessary to deal with the problem related to the calculation of the respective component of the vorticity vector by the difference of the two partial derivations (13). In the area of large velocity gradients, the vorticity evaluation may be subject to large uncertainty, since actually two large numbers, calculated as a proportion of a large and a small number, are subtracted. This fact causes a further increase in the uncertainty of determining vorticity beyond the usual uncertainty in the numerical calculation of the derivative. Because large velocity gradients are usually only in the wall boundary layers with decreasing flow velocity, their real contribution to the quantification of large vortex structure (in terms of influence on angular momentum flux value) is small, insignificant. However, these large gradients have a big influence on the value of vorticity and vorticity numbers.

A possible solution is to exclude the area of the wall boundary layer in the evaluation. The gradual reduction of the influence of vorticity evaluated in the wall boundary layer to vorticity number was monitored – Figure 8, 9 and 10. Vorticity numbers evaluated from area without the wall boundary layer (diameter 76 mm and lower) are almost equal. Practical evaluation of the vorticity numbers is therefore appropriate to calculate in the area reduced by about 1 % of the cylinder diameter.

6. CONCLUSION

The commonly used swirl and tumble number based on angular momentum flux evaluation fail to characterize the level of swirling movements in some cases – for example in case of counter-rotating swirl vortex pair added to dominant tumble motion. Proposed vorticity number can solved this problem because they characterize level of microscopic vortex structure on the scale corresponding to the evaluation mesh size.

However AVG vorticity number calculated as simple sum of appropriate vorticity component provides similar results like from angular momentum flux computed swirl number because it respects rotation direction too. ABS and RMS vorticity number responds correctly, as has been demonstrated by evaluating of two typical in-cylinder flow cases. It is probably more convenient to use the ABS vorticity number because the RMS vorticity number is calculated as the quadratic mean and thus overestimates larger vortices.

Vorticity number can be used as an auxiliary parameter to refine the characterization of intake swirling flow, for example as a correction factor to the standard swirl and tumble numbers. This is especially important in cases when there are two counter-rotating swirl vortices. The way to include vorticity number in the computational models will be the subject of further work.

Both ports, z = 0.6D

0 50 m/s : velocity scale

1 mm

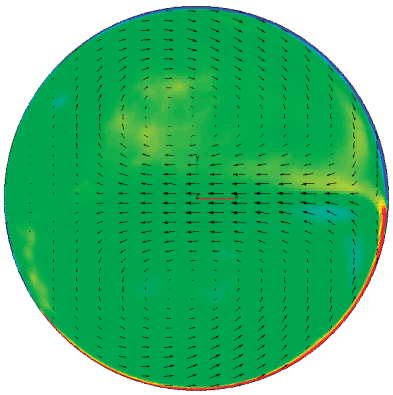

SN = 0.01 VN_{zABS} = 7.75

2 mm

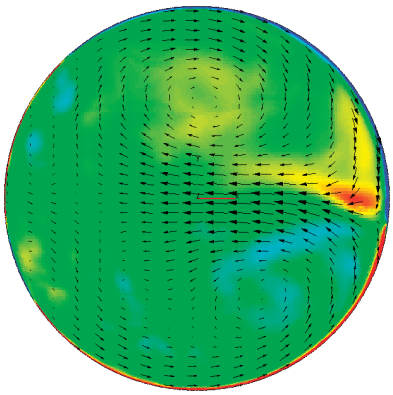

SN = 0.11 VN_{zABS} = 5.04

3 mm

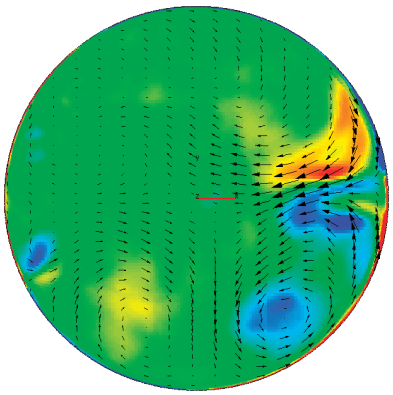

SN = -0.01 V_{NzABS} = 3.90

4 mm

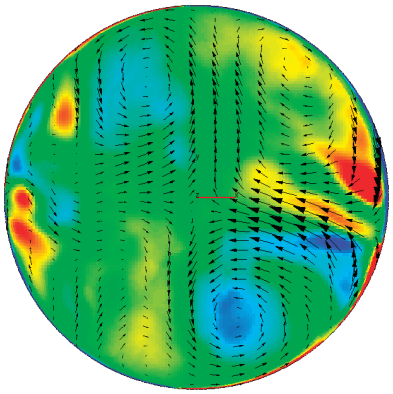

SN = $_{0}$.12 VN_{zABS} = 3.33

5 mm

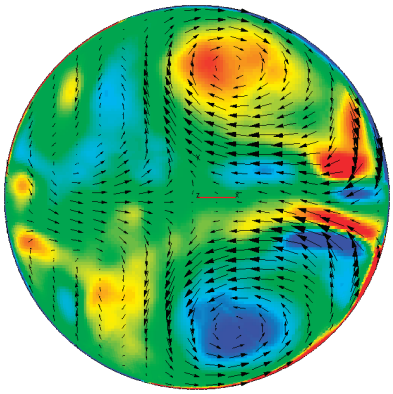

SN = 0.03 VN_{zABS} = 3.21

6 mm

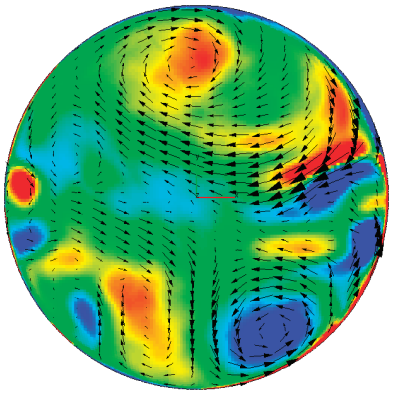

SN = 0.02 VN_{zABS} = 3.01

7 mm

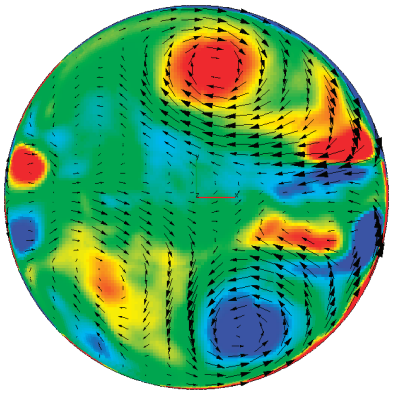

SN = _0.04 VN_{zABS} = 2.70

8 mm

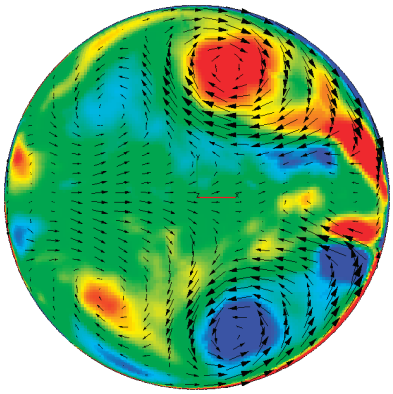

SN = 0.04 VN_{zABS} = 2.88

9 mm

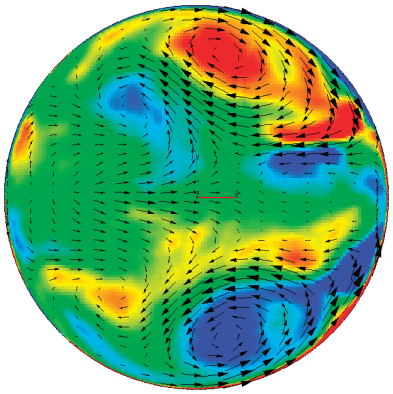

SN = -0.03 VN_{zABS} = 2.79

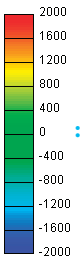

: z-component of vorticity scale

FIGURE 4: Velocity vector field and vorticity z-component (color scale) + swirl number and ABS swirl vorticity number – distance 0.6D from cylinder head, dependence on valve lift – both intake valves being opened

OBRÁZEK 4: Pole vektorů rychlosti a z-ové složky vířivosti + vírové číslo swirlu a ABS vířivostní číslo swirlu – vzdálenost 0.6D od hlavy válce, závislost na zdvihu ventilu – otevřené oba sací ventily.

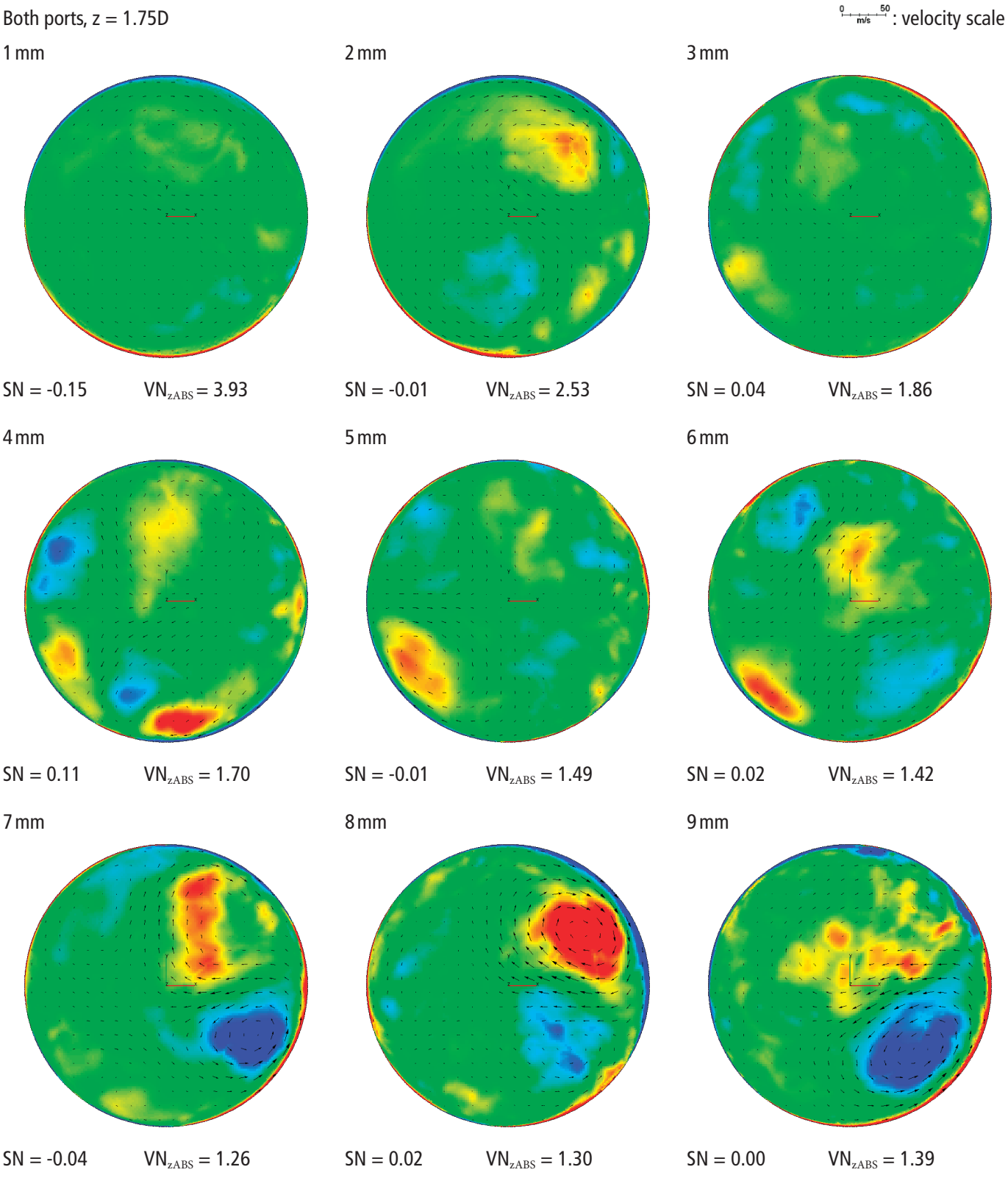

FIGURE 5: Velocity vector field and vorticity z-component (color scale) + swirl number and ABS swirl vorticity number – distance 1.75D from cylinder head, dependence on valve lift – both intake valves being opened

OBRÁZEK 5: Pole vektorů rychlosti a z-ové složky vířivosti + vírové číslo swirlu a ABS vířivostní číslo swirlu – vzdálenost 1.75D od hlavy válce, závislost na zdvihu ventilu – otevřené oba sací ventily.

Single port, z = 0.6D

: velocity scale

1 mm

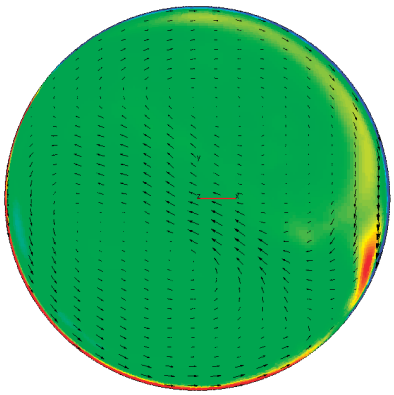

SN = 7.61 VN_{zABS} = 10.94

2 mm

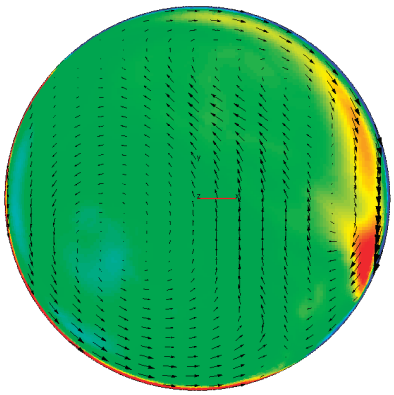

SN = 4.50 VN_{zABS} = 7,27

3 mm

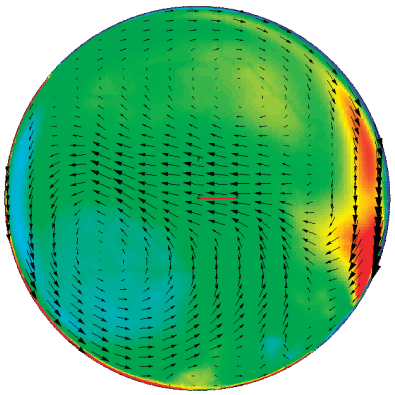

SN = 3.21 VN_{zABS} = 5,44

4 mm

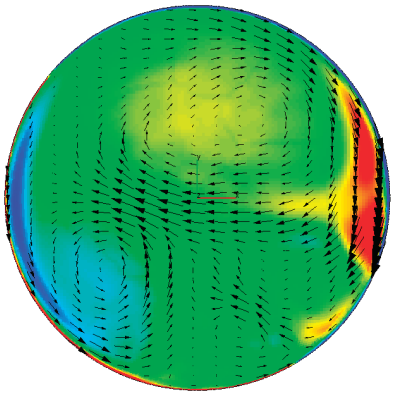

SN = 2,13 VN_{zABS} = 4.69

5 mm

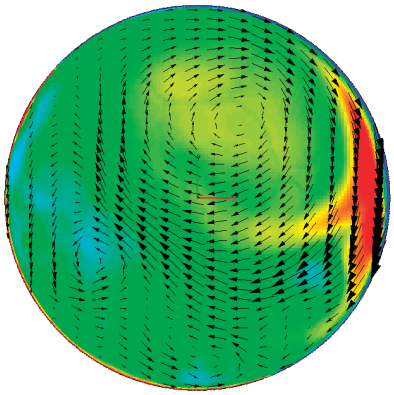

SN = 2,33 VN_{zABS} = 4.28

6 mm

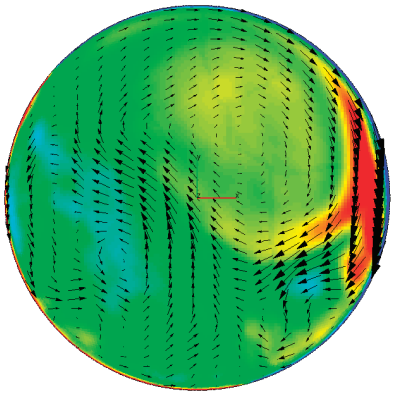

SN = 2,62 VN_{zABS} = 4.10

7 mm

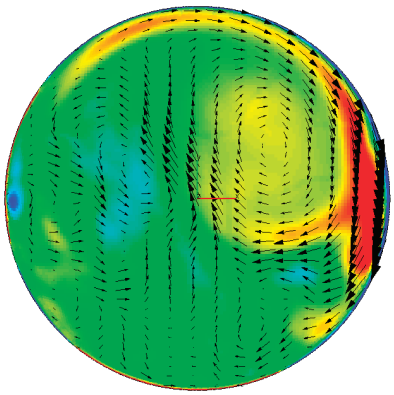

SN = 2,81 VN_{zABS} = 3.94

8 mm

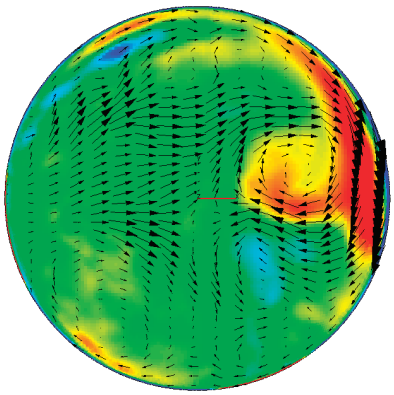

SN = 3,20 VN_{zABS} = 4.23

9 mm

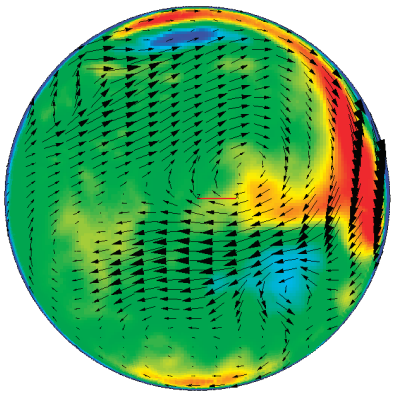

SN = 3,35 VN_{zABS} = 4.44

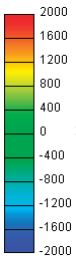

: z-component of vorticity scale

FIGURE 6: Velocity vector field and vorticity z-component (color scale) + swirl number and ABS swirl vorticity number – distance 0.6D from cylinder head, dependence on valve lift – single intake valve being opened.

OBRÁZEK 6: Pole vektorů rychlosti a z-ové složky vířivosti + vírové číslo swirlu a ABS vířivostní číslo swirlu – vzdálenost 0.6D od hlavy válce, závislost na zdvihu ventilu – otevřený jeden sací ventil.

Single port, z = 1.75D

: velocity scale

1 mm

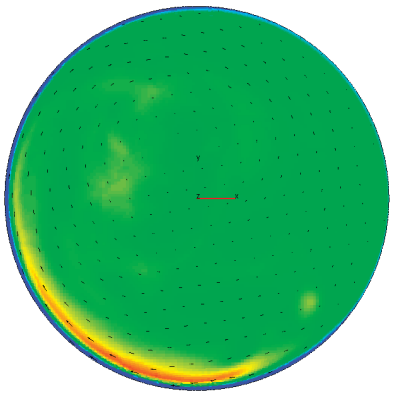

SN = 5.81 VN_{zABS} = 5.58

2 mm

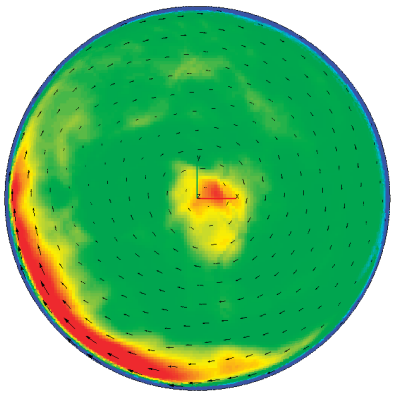

SN = 4.08 VN_{zABS} = 5.15

3 mm

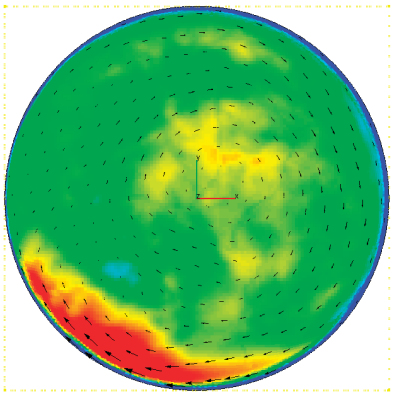

SN = 2.92 VN_{zABS} = 4.68

4 mm

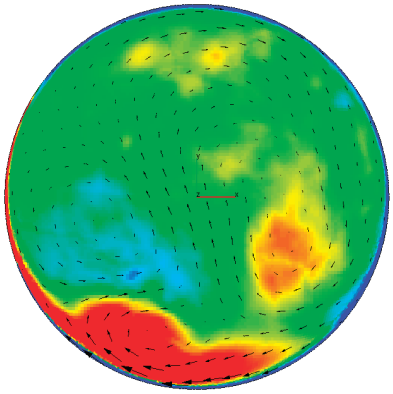

SN = 1.73 VN_{zABS} = 3.74

5 mm

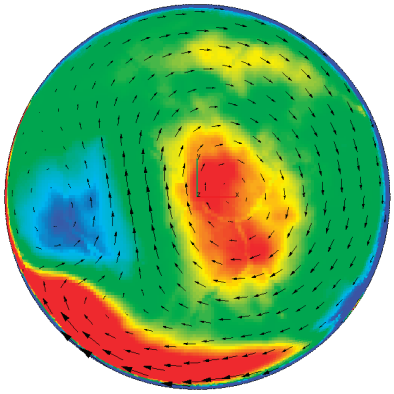

SN = 2.02 VN_{zABS} = 3.51

6 mm

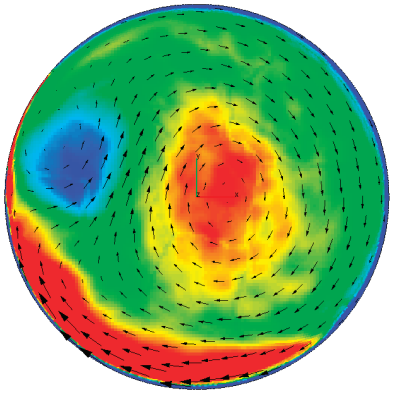

SN = 2.31 VN_{zABS} = 3.42

7 mm

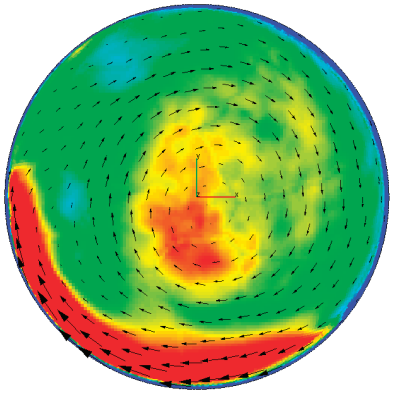

SN = 2.50 VN_{zABS} = 2.71

8 mm

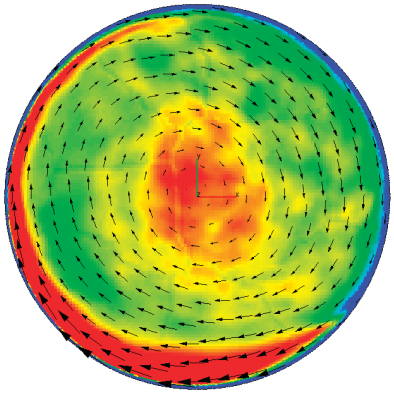

SN = 2.91 VN_{zABS} = 2.84

9 mm

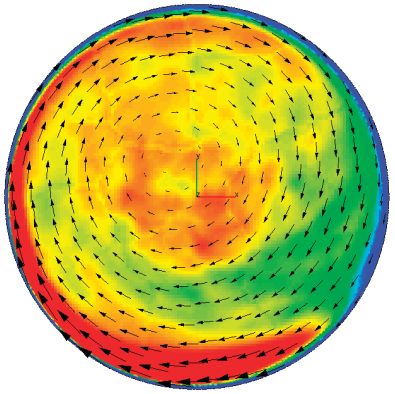

SN = 3.04 VN_{zABS} = 2.78

FIGURE 7: Velocity vector field and vorticity z-component (color scale) + swirl number and ABS swirl vorticity number – distance 1.75D from cylinder head, dependence on valve lift – single intake valve being opened.
OBRÁZEK 7: Pole vektorů rychlosti a z-ové složky vířivosti + vírové číslo swirlu a ABS vířivostní číslo swirlu – vzdálenost 1.75D od hlavy válce, závislost na zdvihu ventilu – otevřený jeden sací ventil.

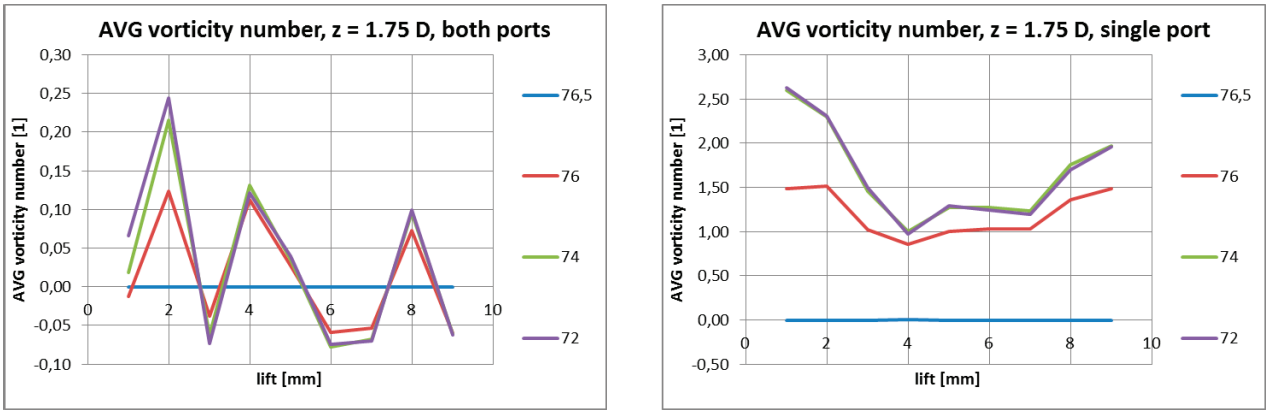

FIGURE 8: AVG swirl vorticity number – dependence on valve lift and max. diameter of evaluation area – the case with both open intake valves is on the left, the case with single open valve is on the right.
OBRÁZEK 8: AVG vířivostní číslo – závislost na zdvihu ventilu a max. průměru vyhodnocovací oblasti – varianta se dvěma otevřenými sacími ventily vlevo, s jedním otevřeným ventilem vpravo.

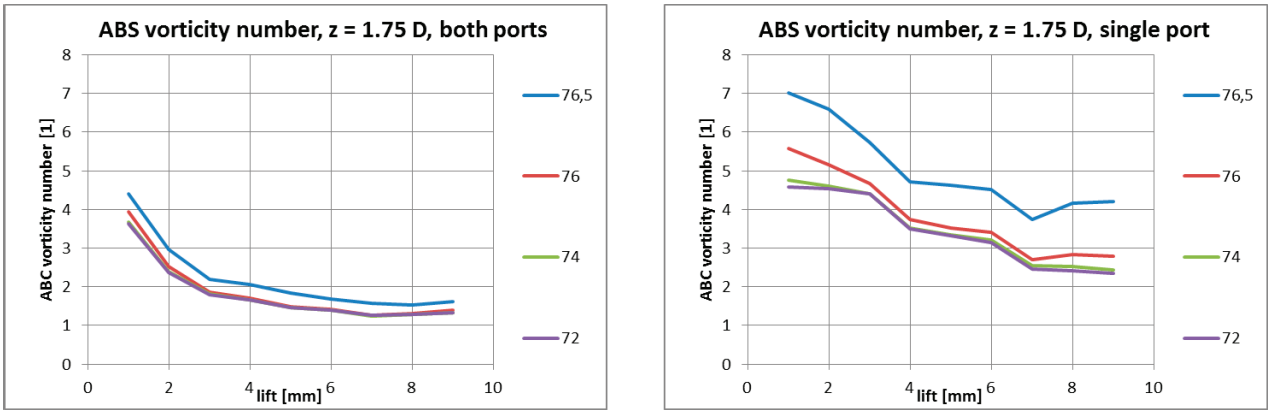

FIGURE 9: ABS swirl vorticity number – dependence on valve lift and max. diameter of evaluation area – the case with both open intake valves is on the left, the case with single open valve is on the right.
OBRÁZEK 9: ABS vířivostní číslo – závislost na zdvihu ventilu a max. průměru vyhodnocovací oblasti – varianta se dvěma otevřenými sacími ventily vlevo, s jedním otevřeným ventilem vpravo.

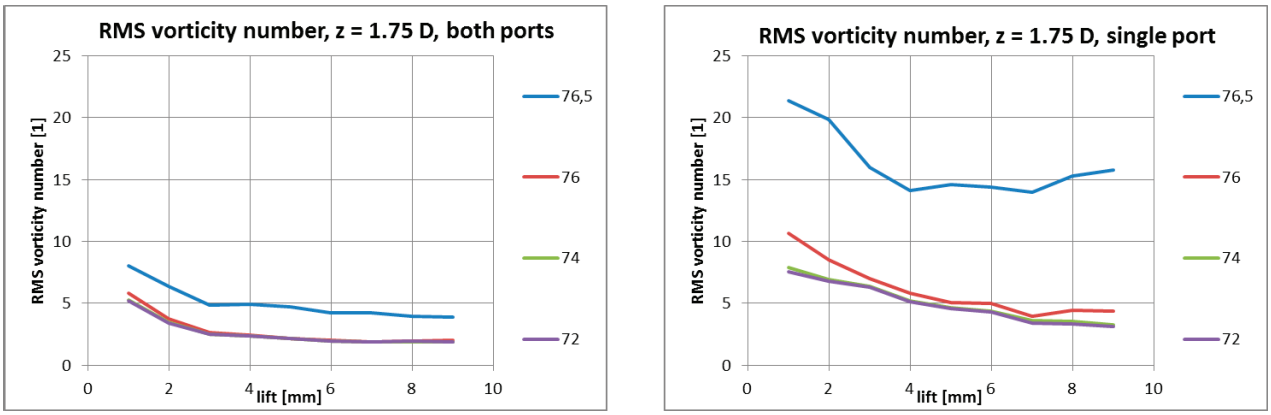

FIGURE 10: RMS swirl vorticity number – dependence on valve lift and max. diameter of evaluation area – the case with both open intake valves is on the left, the case with single open valve is on the right.
OBRÁZEK 10: RMS vířivostní číslo – závislost na zdvihu ventilu a max. průměru vyhodnocovací oblasti – varianta se dvěma otevřenými sacími ventily vlevo, s jedním otevřeným ventilem vpravo.

ACKNOWLEDGEMENTS

This research has been realized using the support of Technological Agency, Czech Republic, programme Centres of Competence, project TE01020020: 'Josef Božek Competence Centre for Automotive Industry'.

This research has been realized using the support of EU Regional Development Fund in OP R&D for Innovations (OP VaVpI) and The Ministry of Education, Youth and Sports, Czech Republic, project CZ.1.05/2.1.00/03.0125: 'Acquisition of Technology for Vehicle Center of Sustainable Mobility'.

This research has been realized using the support of The Ministry of Education, Youth and Sports program NPU I (LO), project LO1311: 'Development of Vehicle Centre of Sustainable Mobility'. All the help has been gratefully appreciated.

LIST OF NOTATIONS AND ABBREVIATIONS

AVG	average
ABS	absolute
RMS	root mean square
CTU	Czech Technical University in Prague
CFD	Computation Fluid Dynamics
ICE	Internal Combustion Engine
PANS	Partially Averaged Navier-Stokes (equation set)
LDA	Laser Doppler Anemometry
PIV	Particle Image Velocimetry

REFERENCES

[1] Hatschbach, P.: Měření rychlostního pole ve válci spalovacího motoru pomocí integrálních metod a laserové dopplerovské anemometrie, Praha: 1995, PhD Thesis. České vysoké učení technické v Praze, Fakulta strojní.

[2] [Jackson, N.S., Stokes, J., Sadler, M., Correlation of the combustion characteristics of spark ignition engines with the in-cylinder flow field characterised using PIV in a water analog rig, SAE paper 971637, 1997

[3] Jaffri, K. – Hascher, H.G. – Novak, M. – Lee, K. – Schock, H. – Bonne, M. – Keller, P. : Tumble and Swirl Quantification within a Motored Four-Valve SI Engine Cylinder Based on 3-D LDV Measurements, SAE 970792,1997

[4] Hatschbach, P.: Quantification of the Vortex Structure in an IC Engine (In Czech), In: Colloquium FLUID DYNAMICS 2004. Praha: AV ČR, Ústav termomechaniky, 2004. pp. 47–50. ISBN 80-85918-89-7.

[5] Huang, R.F., C.W. Huang, S.B. Chang, H.S. Yang, T.W. Lin and W.Y. Hsu (2005). Topological flow evolutions in cylinder of a motored engine during intake and compression stroke. Journal of Fluids and Structures 20, 105–127.

[6] Vitek O., Tichanek R., Hatschbach P.: Application of LES, PANS and RANS to a Case of Intake Channel Steady Flow Test Bench, In: Journal of Middle European Construction and Design of Cars, Vol. 13, No. 3, 2015, pp. 14–23. ISSN W1214-0821

[7] AVL AST (2013). FIRE Manual v2013, AVL List GmbH, Graz.

VEHICLE CENTER OF SUSTAINABLE MOBILITY

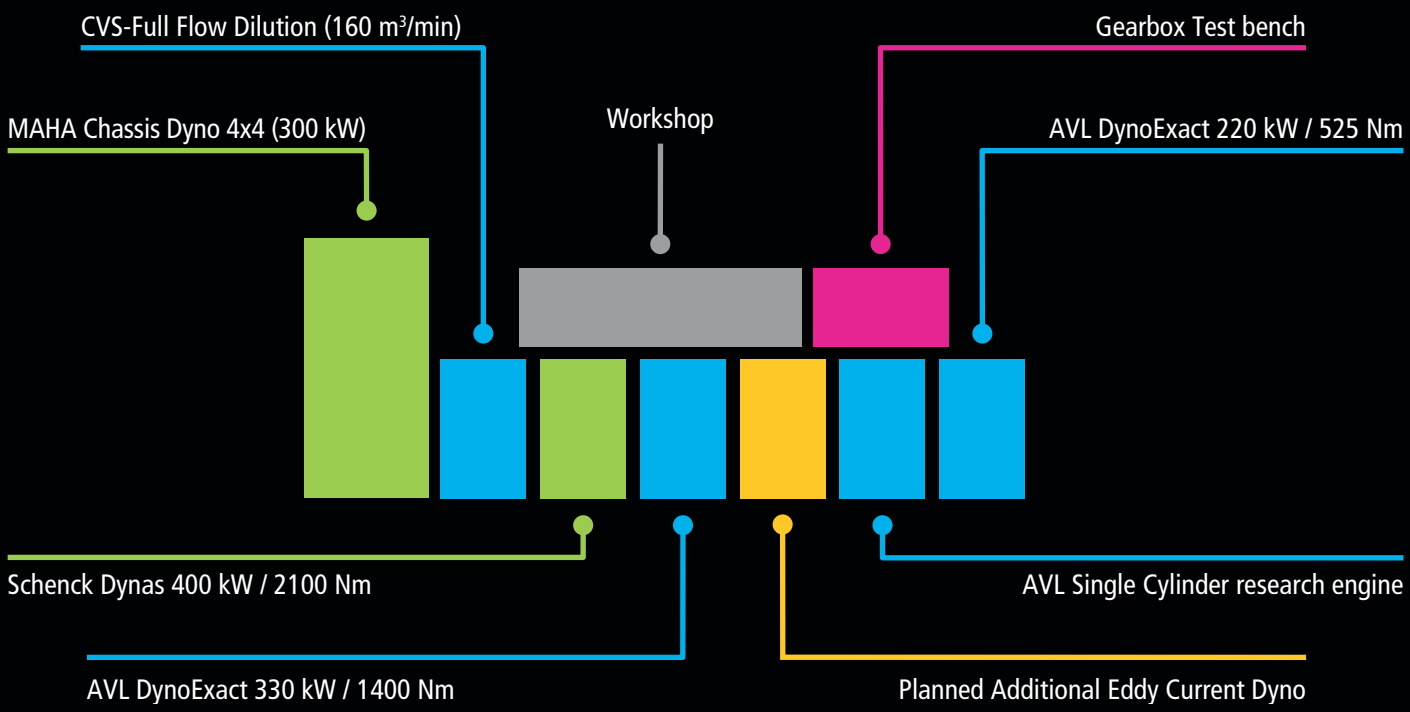

Offers the experimental mearuments and research on the high-end set-ups installed in newly built laboratories in Roztoky (Central Bohemia; 10 kms from Prague). The relevant research workers and postgraduate students of faculties of Mechanical and Electrical Engineering of Czech Technical University in Prague are ready to work on research and development tasks with help of the following experimental equipment:

- 4WD Chassis Dyno
- Two engine test cells with DynoExact and PUMA Automation system
- Compact Single Cylinder Engine TestBed
- Two gearbox test stands
- Equipkent for velocity measurement by Particle Image Velocimetry technique
- Test bench for electric car powertrains
- Laboratory of microelectronics (testing and development of vehicle distributed systems, EMC of distributed systems, X-by-wire systems)
- Laser Scanning Vibrometer

For any further information please contact:
BOHUMIL MAREŠ
VTP Roztoky, Přílepská 1920, 252 63 Roztoky
E-mail: bohumil.mares@fs.cvut.cz

Acquisition of Technology for Vehicle Center of Sustainable Mobility CZ.1.05/2.1.00/03.0125

CZECH TECHNICAL UNIVERSITY IN PRAGUE
CENTRUM VOZIDEL UDRŽITELNÉ MOBILITY
MINISTERSTVO ŠKOLSTVÍ, MLÁDEŽE A TĚLOVÝCHOVY
EVROPSKÁ UNIE
EVROPSKÝ FOND PRO REGIONÁLNÍ ROZVOJ
INVESTICE DO VAŠÍ BUDOUCNOSTI
OP Výzkum a vývoj pro inovace

GUIDELINES FOR AUTHORS

A. LANGUAGE

01) Language of paper – American English
02) Abstract, captions and keywords will be bilingual English and Czech, optionally English and Slovak. Authors from the Czech and Slovak Republic should prepare abstract, keywords and captions in English and native language. The abstract and captions for other authors will be translated by the publisher to Czech language.

B. LENGTH

Title should not exceed 10 words
Subtitle should not exceed 15 words
Abstract should not exceed 200 words
Paper without limit

C. ORDER OF CONTENTS

01) Title
02) Author(s) name: per author company/institute, address, and e-mail (on new line)
03) Abstract
04) Keywords
05) Body of the paper. The paper should be divided into logical numbered sections.
06) Preferred structure:
    – Introduction: Background – Motivation – Goals
    – Used methods
    – Results
    – Analysis of results and evaluation
    – Conclusion: Result Utilization – Prospects
07) Acknowledgements
08) List of notations and abbreviations (in alphabetical order)
09) References
10) Appendices: Long derivation of equations, description and parameters of experimental equipment or methods, etc.

To facilitate the blind reviewing process, the authors are asked provide on a separate first page the items 1) and 2) and to start the main part of the article with 1) Title; and then 3) Abstract, and so on.

D. GRAPHICAL ARRANGEMENT

Title: Times New Roman 17b, Bold
Body of paper, abstract, equation numbering: Times New Roman 11b. Titles of sections Times New Roman 12b Bold. Symbols of physical quantities used in text: italic. SI units, wherever possible. Combined units should be written with dot (example: N.m, $m.s^{-2}$, …).
Authors should avoid the usage of footnotes.
Captions: Times New Roman 10b, in bold – number and caption, normal – text of legend. See examples:

Figure 1: This is a figure.
Table 1: This is a table.

All illustrations should be numbered sequentially with arabic numbers.
Equations: Times New Roman italic. Variable 12b, Index 7b, Small index 5b, Symbol 18b, Small symbol 12b. Mathematical operators and constants (Ex.: sin, e, π, …) Times New Roman 12b normal.
All equations should be numbered sequentially with arabic numbers. List of notations either under every equation, or at the end of paper – see paragraph D (according to number and content of equations). Long derivation as appendix on the end of paper.
References: References referred in text in square brackets in format of text (Ex: [1])
Format of references, examples:

[1] Author A., Author B. and Author C. (2002). This is journal article, In: Journal for Interesting Papers, Vol. 10, No. 3, p. 130–145. ISSN
[2] Author A., Author B. and Author C. (eds.). Our Book on Car Technology, MIT Press, Massachusetts, 2002, p. 23-145. ISBN
[3] Author A., Author B. and Author C. (2002). My paper in a conference, In: Editor A., Editor B. and Editor C. (eds.). Proceedings Of Our Meeting in a Far Away Exotic Place, MIT Press, Massachusetts, p. 78-89. ISBN

E. ILLUSTRATIONS

The Journal is full-color.
The authors are responsible for delivering high-quality graphic material. In the case of illustrations sent via mail, the orientation of illustrations should be indicated, as well as their number in the article. The illustrations sent electronically, should be sent in the correct orientation and in a resolution at least 300 dpi, in common graphical formats.

F. SUBMISSION OF MANUSCRIPTS

Text should be in all cases prepared in electronical form. Paper can be sent via mail (the contents of mail should be illustrations and diskette 3,5" or CD with text), or via e-mail on the address mentioned below.
Text should be sent in format MS Word 2000 or older (format doc, or rtf). Do not merge illustrations in the text to avoid excessive file size. All illustrations should be sent in separate files. No illustrations will be returned unless specifically requested.
Contact address for submission of paper:
ČVUT, FS, MECCA
Gabriela Achtenová
Technická 4, 166 07 Praha 6, Czech Republic
Tel.: +420 2 24 35 24 99, Fax: +420 2 24 35 25 00
E-mail: gabriela.achtenova@fs.cvut.cz

G. COPYRIGHT

The papers submitted to journal MECCA have not been previously published or submitted elsewhere. The copyright of accepted papers becomes the property of Czech Technical University, and usage of any part of papers without permission of Czech Technical University will be not allowed. Authors who wish to reproduce already published illustrations should asked the permission by the copyright holder. Authors are asked to sign copyright agreement.

H. PUBLICATION

All articles will be blind reviewed. The first author, if no other contact person is marked, will be informed about the decision as soon as possible.
Authors will get 3 copies of the journal in which the article is published.

MASTER OF AUTOMOTIVE ENGINEERING

ENTRANCE LEVEL: Technical bachelor (mechanical, transport, or electro engineering)

CTU
Prague
Czech republic

(E)

ITB
Bandung
Indonesia

(E), (I)

ENSTA
Brest
France

(F)

TUCH
Chemnitz
Germany

(G)

3rd SEMESTER

Entrance exam IFP

ENSTA
- Design of Vehicles
- Modelisation and Computation

(F)

HAN
Vehicle Dynamics and Intelligent Transport Systems

(E)

CTU
Advanced Powertrains

(E)

TUCH
Alternative Powertrains

(G)

IFP
Paris
France

(F)+(E)

4th SEMESTER devoted to final thesis and 5 months internship in an industrial or academic environment anywhere in the world

MASTER DEGREE IN AUTOMOTIVE ENGINEERING
Master degree from 2 countries with respect to chosen specialisation in 3rd semester

(F) – in French, (E) – in English, (I) – in Indonesian, (G) – in German

CTU
Czech Technical University in Prague
Czech Republic
Gabriela Achtenová
gabriela.achtenova@fs.cvut.cz
Tel.: +420 224 352 499

ITB
Institut Teknologi Bandung
Indonesia
Andi Isra Mahyuddin
aim@ftmd.itb.ac.id

ENSTA
ENSTA Bretagne
France
Yann Marco
yann.marco@ensta-bretagne.fr
Tel.: +33 298 348 844

TUCH
Technische Universität Chemnitz
Germany
Martin Hipp
martin.hipp@mb.tu-chemnitz.de
Tel.: +49 371 531 337 94

HAN
Hogeschool van Arnhem en Nijmegen
The Netherlands
Kea Bouwman
kea.bouwman@han.nl
Tel.: + 31 26 384 93 14

DEADLINE FOR EU AND NON EU STUDENTS 1st MAY 2022
For application form, detailed programme, studying conditions, tuition fees and all other informations, please see: www.emae.eu

CZECH TECHNICAL UNIVERSITY IN PRAGUE
INSTITUT TEKNOLOGI BANDUNG 1920
ifp SCHOOL
ENSTA Bretagne
TECHNISCHE UNIVERSITÄT CHEMNITZ
Hogeschool van Arnhem en Nijmegen HAN University